



Cite this: *Biomater. Sci.*, 2025, **13**, 5442

Seeing deep to map cell–biomaterial interactions via whole mount light sheet imaging and automated analytics in decellularized extracellular matrix models

Oscar R. Benavides,^{†,a} Sabrina N. VandenHeuvel,^{†,a} Sanjana Roy,^a Brinlee Goggans,^{†,a} Shubha Holla,^{†,a} Varsha Rajavel,^a Joseph Duran,^a Lucia L. Nash,^a Daniel L. Alge,^{†,a} Alex J. Walsh^{*a} and Shreya A. Raghavan ^{†,a,b}

In vitro models aim to improve biomimicry of *in vivo* tissues and disease processes. Decellularized extracellular matrix (dECM) scaffolds mimic cellular interactions with 3D tissue architecture. These complex 3D models require parallel advancements in analytical methods to quantify functional outputs with respect to scaffold architecture and recellularization while retaining spatial integrity. Current imaging methods optimized in other engineered model systems are limited in their application to dECM due to the inherent thickness, high heterogeneity, opacity and autofluorescence of dECM material. Sacrificial sample preparation methods like digestion and tissue sectioning are tedious and reduce the amount of spatially relevant information that can be extracted. Further, imaging depth and resolution are limited due to light scattering within large opaque scaffolds. We aimed to optimize optical imaging and analysis protocols to overcome imaging challenges and enable quantitative assessments of dECM models, demonstrating a use case in engineered *in vitro* cancer microenvironments. We first combined a series of established sample preparation methods including tissue clearing agents and cell labeling dyes, to optimize dECM scaffold compatibility with volumetric light sheet fluorescence microscopy (LSFM) imaging. We then developed image analysis algorithms capable of overcoming the segmentation limitations of established methods to accurately quantify scaffold porosity as well as cellular occupation and migration at the single cell level within dECM scaffolds. We automated this analysis to increase usability for large data sets and applied the imaging methods to a porcine liver-derived dECM scaffold model, called a biomatrix. Biomatrices recellularized with colorectal cancer spheroids model liver metastasis. The LSFM imaging and analysis successfully detected increased cell numbers between 3 and 5 days of culture on the dECM biomatrix, and the loss of cells in oxaliplatin-treated biomatrices. With the ability to resolve these key changes in proliferation, invasion and therapeutic response, this optimized set of imaging and computational tools will aid in the mechanistic and therapeutic discovery of colorectal cancer liver metastasis. Broadly, the increased volume and resolution of imaging data from our methods can extract spatially relevant scaffold and cellular information within the context of any dECM model, increasing its adoptability to probe complex biological behaviors across diseases.

Received 23rd April 2025,
Accepted 7th August 2025

DOI: 10.1039/d5bm00630a
rsc.li/biomaterials-science

1 Introduction

Comprehensive characterization of complex, biomimetic *in vitro* models is paramount for advancing knowledge of

disease mechanisms and developing novel therapies. Biomaterials models like decellularized extracellular matrix (dECM) scaffolds hold significant promise in areas such as cancer discovery and tissue engineering,^{1–6} yet their effective utilization hinges on the availability of advanced analytical tools. The application of dECM models to metastatic cancer discovery is of particular interest.^{7–13} In dECM metastatic cancer models, cancer cells are seeded onto and migrate within scaffolds to mimic metastatic organ colonization. To analyze hallmark metastatic behavior within such models, precise quantification of changes in nest size and invasion depth over time are paramount. Unfortunately, the large size,

^aDepartment of Biomedical Engineering, Texas A&M University, 3120 TAMU, 5016 Emerging Technologies Building, 5032 Emerging Technologies Building, College Station, TX 77843, USA. E-mail: walshaj@tamu.edu, sraghavan@tamu.edu; Tel: +1 979-458-3126, +1 979-845-5540

^bCPRIT Regional Excellence Center in Cancer at Texas A&M University, College Station, TX, USA

[†]These authors contributed equally.



opacity and nonuniform architecture of dECM scaffolds make this characterization difficult. On account of resolution and adaptability limits, available imaging and image analysis methods are insufficient to identify subtle but key differences in the context of cancer progression.^{13,14}

We previously developed a porcine liver dECM scaffold, called a biomatrix, that maintained physiological porosity and stiffness of native tissue with no detectable native porcine DNA. These liver biomatrices were repopulated with colorectal cancer cell clusters (spheroids) to model and investigate metastatic behavior in bioengineered colorectal cancer liver metastases (CRLM).¹ In the engineered CRLM model, spheroids colonized the biomatrix and adopted mesenchymal, invasive genotypes and resistance to chemotherapy.¹ In addition to molecular genotyping, invasion and colonization of the biomatrix were assessed using multiphoton microscopy (MPM) and second harmonic generation (SHG) imaging. The integration of these optical imaging methods into cancer engineering allowed quantification of metastatic colonization in the dECM liver biomatrix. However, the impact of MPM and SHG imaging was limited by weak optical signals leading to low resolution, slow acquisition speeds (>1 hour) restricting feasibility and scalability, and an imaging depth of only ~100 μm below the biomatrix surface due to high scattering of the tissues.¹ These barriers prevented the analysis of MPM data from resolving any differences in cancer cell invasion into the biomatrix; furthermore SHG data also did not provide any architectural insights into the dECM biomatrix itself.¹

Toward addressing these limitations, this study presents optimized sample processing, imaging, and analysis techniques for 3D volumetric visualization and quantification of biomatrix architecture and cells. The power of the integrated microscopy and analysis techniques is demonstrated using our previously established dECM-based engineered CRLM model. Composed of decellularized porcine liver biomatrices repopulated with 3D cancer spheroids, the engineered CRLM model mimics the physiological process of metastatic nest formation from circulating tumor cells *in vivo*.^{1,15,16} Our early work demonstrated this model's potential for therapeutic screening, even when examined with the previously limited analytical methods. Motivated by these promising implications, we began developing an improved optical imaging and analysis pipeline with the goal of more precisely visualizing and quantifying ECM architecture and cellular behavior throughout the 3D volume of dECM biomatrices. We hypothesized that uniquely combining and optimizing sample preparation and imaging techniques with a custom analysis platform would enable extraction of porosity, colonization and invasion information, thereby improving understanding of metastasis and novel therapeutic strategies for CRLM. We demonstrated the power of light sheet fluorescence microscopy (LSFM), in combination with our custom image analysis program, to evaluate progressive colorectal cancer by resolving expected time-dependent growth and invasion kinetics and loss of cells in response to chemotherapy. Importantly, the multi-step analysis procedure was automated for feasibility with large datasets pro-

duced by dECM models. With the improved ability to characterize dECM and detect spatial variations in cellular behavior with limited user time demand, the presented techniques offer an avenue to extract valuable spatial information of cell-biomaterial interactions which has been otherwise limited or difficult to obtain using previous methods. As such, we expect they can increase the utility and diversify the implementation of dECM models for cancer and other applications.

2 Materials and methods

2.1 Materials

The HCT116 human colorectal cancer cell line was purchased from American Type Culture Collection (ATCC; Manassas, VA). All cell culture and tissue processing reagents were supplied by ThermoFisher Scientific (Waltham, MA) unless otherwise specified. Fetal bovine serum (FBS) was purchased from Peak Serum (Bradenton, FL), Nycodenz from Serumwerk (Bernburg, Germany), and dichloromethane, ethyl cinnamate (EC), and pepsin from Sigma Aldrich (St Louis, MO).

2.2 Tissue decellularization

Whole porcine livers were donated in excess by Rosenthal Meat Science and Technology Center in the Department of Animal Science at Texas A&M University. Decellularized extracellular matrix (dECM) scaffolds (biomatrices) were generated from 1–2 whole livers *via* previously reported methods used to establish the biomimetic metastasis model.¹ dECM biomatrices are engineered by whole porcine liver sectioning and decellularization through a 9-day series of agitated washes conducted at 4 °C, with solutions changed daily as summarized by Fig. 1A. Liver sections were washed for 3 days with water, followed by 3 days in detergent (1% Triton X-100, 0.1% ammonium hydroxide). Enzymatic digestion of remaining cellular DNA was achieved through a 1-hour static incubation with 1 U mL⁻¹ DNase treatment at 37 °C, and a final 3 days in water washed away decellularization reagents prior to lyophilization. For characterization, liver tissue sections were paused at each stage of the decellularization process and were analyzed fresh for biochemical composition or fixed for imaging.

2.3 Biomatrix characterization

Decellularization was confirmed by quantification of DNA isolated from minced tissue samples (fresh liver or dECM biomatrix) following manufacturer's tissue-specific protocols for the QIAamp DNA micro kit (Qiagen, Hilden, Germany). DNA concentrations were normalized to tissue wet weight prior to mincing and isolation to produce ng μL^{-1} mg⁻¹ values. Swelling was assessed by immersing biomatrices in deionized water for 24 hours and comparing the mass from the dry state to final swelled state after pat drying.

Biochemical analysis was conducted on fresh or decellularized liver digested for 5–9 days with 1 mg mL⁻¹ pepsin in 0.01 M HCl. Digested samples were spun to pellet any undigested material, and the supernatant was characterized. Total protein



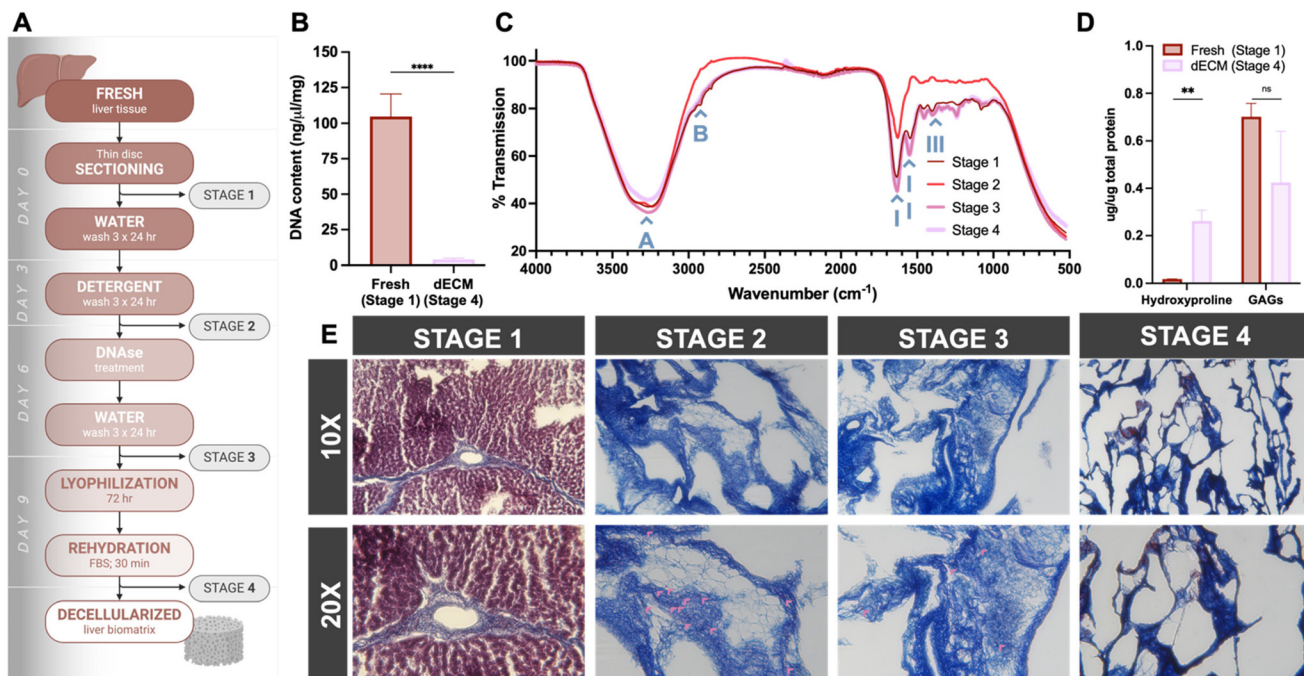


Fig. 1 Tissue decellularization and biomatrix characterization. (A) Schematic of porcine liver decellularization process to produce biomatrices. For biomatrix characterization, samples were paused after initial sectioning (stage 1), washing and detergent treatment (stage 2), enzymatic digestion (stage 3) and lyophilization and rehydration (stage 4). (B) Decellularization efficiently reduced DNA content from $104.8 \pm 15.63 \text{ ng } \mu\text{L}^{-1} \text{ mg}^{-1}$ in fresh liver (stage 1) to $3.86 \pm 1.00 \text{ ng } \mu\text{L}^{-1} \text{ mg}^{-1}$ in the liver biomatrix (stage 4). (C) FTIR spectra demonstrate that the collagen network of native liver tissue (stage 1) was preserved throughout the decellularization process. The rehydrated dECM biomatrix (stage 4) produced an FTIR spectrum characteristic of collagen with key absorption bands at amide I ($\sim 1630 \text{ cm}^{-1}$), amide II ($\sim 1555 \text{ cm}^{-1}$), amide III ($\sim 1260 \text{ cm}^{-1}$), amide A (3200–3400 cm^{-1}) and amide B ($\sim 2920 \text{ cm}^{-1}$) indicated by the blue arrows. (D) Hydroxyproline and GAGs were both detected in dECM biomatrices. Fresh liver tissue (stage 1) is largely comprised of cells, leading to low hydroxyproline levels ($1.79 \pm 0.08\%$ of total protein) which increased significantly in dECM samples (stage 4) to $26.13 \pm 4.63\%$ (** $p < 0.01$, unpaired t test). GAG content was maintained through decellularization (compare $0.70 \pm 0.06 \mu\text{g}$ GAGs per μg total protein at stage 1 to $0.42 \pm 0.22 \mu\text{g}$ μg^{-1} at stage 4; ns, unpaired t test). (E) Representative images of trichrome-stained sections show the presence of collagen fibers (blue) which are surrounded by cells (red) in fresh tissue (stage 1). Large cell areas are removed by stage 2 with some examples of residual cellular material indicated by the pink arrows. Nearly all residual red stain is gone by stage 3 indicating the successful removal of cells. The interconnected, porous architecture of the collagen appears to be upheld throughout the decellularization process (stages 2–4) with slight visually apparent compacting of collagen fiber structures upon lyophilization in stage 4.

content was measured using the Pierce BCA protein assay kit before targeted analysis with the hydroxyproline and glycosaminoglycans (GAGs) assay kits from Chondrex, Inc. (Woodinville, WA) following manufacturer's protocols. For hydroxyproline quantification, the samples were hydrolyzed in 10 N HCl at 120 °C for 24 hours. The hydrolysates were mixed with 1× Chloramine T and incubated for 20 minutes at room temperature. Subsequently, 1× DMAB (4-dimethylaminobenzaldehyde) was added and incubated for 30 minutes at 60 °C. Absorbance was read at 560 nm on an Epoch2 Absorbance Microplate Reader using Gen5 software (BioTek Instruments, Winooski, VT), and compared to a standard curve to quantify hydroxyproline content. GAG content was determined using a DMB (1,9-dimethylmethylene blue) solution to quantify sulfated GAGs with a chondroitin sulfate standard. Absorbance measurements were collected within 5 minutes of mixing samples with the dye solution at 530 nm.

For Fourier transform infrared spectroscopy (FTIR), samples were air dried and analyzed with a Nicolet 380 FTIR spectrometer (ThermoFisher Scientific). The system acquired

64 scans with 1.929 cm^{-1} resolution in transmission mode. The EZ OMNIC software was used to acquire and identify peaks in the FTIR spectra data.

For imaging, samples were fixed with 4% paraformaldehyde (PFA; Santa Cruz Biotechnology, Dallas, TX) solution prior to paraffin embedding and sectioning by the Veterinary Medicine and Biomedical Sciences Core Histology Lab (RRID: SCR_022201). Slides containing 20 μm -thick sections were deparaffinized with xylene and stained using a Masson's trichrome stain kit (StatLab Medical Products; McKinney, TX). Representative images were taken on an inverted microscope fitted with the AmScope MU 20.0MP Camera (AmScope, Irvine, CA).

2.4 Cell culture

HCT116 cells were cultured in Dulbecco's Modified Eagle Medium (DMEM) supplemented with 10% heat-inactivated FBS and 1× antibiotic-antimycotic solution. A lentivirus encoding the mCherry fluorescent protein (Genecopoeia, Rockville, MD) was used to transduce the cells for imaging purposes,



following protocols established previously.¹⁷ From standard monolayer culture, 100 HCT116^{mCherry} cells were seeded into each well of a hanging drop array and cultured for 4 days to generate 3D spheroids.¹⁸

2.5 Generation and monitoring of engineered colorectal cancer liver metastasis (CRLM)

Previous work in our lab confirmed the ability to use compact tumor spheroids to generate *in vitro* CRLM within decellularized liver biomatrices.¹ Day 4 colorectal cancer spheroids were mechanically dissociated into small clusters and seeded at a density of 20 spheroids/0.5 mg biomatrix onto 0.50–1.00 mg (dry weight) sections of liver biomatrix. CRLM samples were maintained for up to 5 days with media replacement on day 3. On day 3, media was removed from all CRLM biomatrices and replaced with either fresh media (control) or media containing 500 μ M oxaliplatin (MedChem Express, Monmouth Junction, NJ).

An MTS viability assay (Abcam, Cambridge, UK) was performed to evaluate successful biomatrix colonization by cancer cells as well as proliferation over time. At each timepoint of interest (days 0, 3, 5), CRLM biomatrices were transferred to individual wells of a 96-well plate containing the MTS reagent and complete culture medium (1:10). After a 2-hour incubation at 37 °C, absorbance was measured at 490 nm on a Cytaion 7 Microplate Reader (BioTek Instruments). Absorbance measurements taken on day 0 were averaged for each experiment and used to normalize all succeeding day 3 and 5 measurements to report fold change in proliferation over time. Proliferation data were visually validated by scanning electron microscopy (SEM). To prepare for SEM, CRLM biomatrices were subjected to overnight fixation in 4% PFA at 4 °C prior to dehydration by a graded ethanol series and lyophilization. Finally, gold coating was performed using a Cressington Vacuum Sputter Coater 108 (Ted Pella, Inc., Redding, CA) to produce highly conductive samples for imaging with a Quanta 600 field emission-scanning electron microscope (FEI Company, Hillsboro, OR).

2.6 Optical clearing of CRLM scaffolds

A modified iDISCO+ (Immunolabeling-enabled three-Dimensional Imaging of Solvent-Cleared Organs) procedure^{19–21} was optimized and performed starting with a methanol/H₂O dehydration series. Clearing was achieved with a 6-hour incubation in a solution of 66% dichloromethane/33% methanol at room temperature with gentle shaking. Finally, the samples were transferred to ethyl cinnamate (EC) for refractive index matching and imaging. Matching was achieved with overnight incubation on a tube rotator at room temperature, and samples were subsequently stored in EC at room temperature until imaging.

To analyze clearing methods, uncleared biomatrices were compared to those cleared with either the previously used refractive index matching solution (RIMS)¹ or the iDISCO+/EC procedure. For RIMS, fixed samples were simply submerged in a Nycodenz/phosphate buffer solution and equilibrated at

least overnight.²² Empty biomatrices (not seeded with spheroids) cleared with each method were imaged with light sheet fluorescence microscopy (LSFM; section 2.9) in the corresponding immersion medium. The central slice of the image stack was chosen for analysis of maximum imaging depth. An intensity profile was plotted in ImageJ to visualize contrast and resolution with depth.

2.7 Confocal fluorescence microscopy of CRLM

Confocal fluorescence microscopy of CRLM biomatrices was performed using a Leica SP8 confocal fluorescence microscope (Leica Microsystems, Wetzlar, Germany) with a 10 \times 0.40 NA objective lens. Biomatrices were placed on a microscope slide in an orientation such that they would have minimal depth. A coverslip was not placed on the biomatrix to avoid compression of the dECM architecture and cell morphology. The mCherry fluorophore was excited at an illumination wavelength of 585 nm and imaged at 600–700 nm. Volumes were acquired using the full objective travel range (500 μ m).

2.8 Cellular labeling with BioTracker 655 nm cytoplasmic membrane dye and DAPI nuclear stain

After culturing, fixation, clearing, and imaging of mCherry⁺ CRLM biomatrices, increased signal intensity and image contrast were desired to aid in cell segmentation. Samples were subsequently stained with BioTracker 655 nm Red Cytoplasmic Membrane Dye (Sigma Aldrich) according to the manufacturer's protocol to increase the detectable fluorescent signal as endogenous fluorescence was apparently quenched through the clearing process. Briefly, cleared CRLM biomatrices were incubated in 500 μ L EC mixed with 1 μ L of BioTracker for 1 hour at 37 °C on a tube rotator. Following a 10-minute static incubation at room temperature to allow biomatrices to settle by gravity, the solution was removed and replaced with fresh EC for another 10 minutes at 37 °C with rotation. Three EC washes were completed in total. To confirm the accuracy of BioTracker dye labeling, CRLM samples were additionally stained with 1 μ g mL⁻¹ DAPI (4',6-diamidino-2-phenylindole) nuclear stain.

2.9 Light sheet fluorescence microscopy (LSFM) of CRLM

LSFM of CRLM biomatrices was performed using a ZEISS Z.7 light sheet microscope (ZEISS Microscopy, Oberkochen, Germany) with 5 \times 0.1 NA illumination and 5 \times 0.16 NA detection objective lenses. All biomatrices were imaged using EC as the immersion medium and the objective lens correction collar was set accordingly ($n = 1.56$). All LSFM volumes were acquired using the central 1000 \times 1920 (XY) pixels, dual sided illumination and pivot scanning for uniform illumination and axial resolution across the 3D volume. A 0.52 \times optical zoom (*i.e.* 2.6 \times effective magnification) was used to achieve isotropic 1.79³ μ m³ voxels.

Volumes targeting mCherry contrast were acquired before BioTracker labeling. mCherry was illuminated with 561 nm and detected with a 585+ nm emission filter. An illumination power of 40–50 mW (laser output) and camera integration time



of 100 ms per frame were used to image mCherry and fill the 16-bit camera dynamic range. Conversely, BioTracker was illuminated with 638 nm and detected with a 660+ nm filter. Approximately 1.5 mW of 638 nm excitation power (laser output) was used to excite the BioTracker dye with an integration time of 20 ms per frame. For DAPI visualization, samples were illuminated with 25 mW of 405 nm excitation power and detected with a 420–470 nm emission filter. Cells and the biomatrix architecture were imaged simultaneously for each sample. For this reason, dECM autofluorescence signal was collected using varied excitation and emission wavelengths, depending on the corresponding wavelengths needed for cell fluorescent labels within the scaffolds. For empty biomatrix samples used to assess optical clearing, autofluorescence was illuminated with 561 nm and detected with the 585+ nm emission filter using an illumination power of 20 mW (laser output) and camera integration time of 100–150 ms per frame.

2.10 Biomatrix scaffold segmentation and porosity

LSFM volumes were acquired with 5% pixel overlap for manual stitching with Imaris image analysis software (Oxford Instruments, Abingdon, UK) and converted to 16-bit TIFF files. 2D image stacks were pre-processed in MATLAB (MathWorks, Natick, MA) to increase fluorescence contrast of the scaffold throughout the stitched LSFM volume. The biomatrix structure was then segmented using a series of image filters in MATLAB. A Hessian-based filter was applied to identify ridge-like features, followed by binarization using a high-pass filter and an additional high-pass filter to remove small segmented but disconnected objects to produce the final segmented biomatrix. The total volume of the biomatrix envelope (*i.e.* biomatrix convex hull) was then also segmented with a series of morphological dilation, erosion, and flood-fill operations. The total volumes (μm^3) of each biomatrix (ECM-occupied space) and envelope (total volume of biomatrix with pores) were calculated by multiplying the number of binarized voxels of each channel with the voxel volume. Porosity was quantified using the following equation:

$$\text{Porosity (\%)} = \left(1 - \frac{\text{biomatrix volume}}{\text{envelope volume}} \right) \times 100. \quad (1)$$

2.11 Processing of LSFM volumes for quantitative image analysis of 3D dECM biomatrix cellular invasion

For segmentation of cells, stitched 3D volume TIFFs were pre-processed in ImageJ to increase the contrast of cells from deep planes within the biomatrix. The contrast-enhanced volumes underwent high-pass Fourier transform filtering before being binarized using the global thresholding IsoData method.²³ A watershed transformation was performed to split touching objects. Cell-segmented 3D TIFF volumes were converted to .ims files for cell invasion analysis in Imaris.

Graph-cut segmentation was performed using the Image Segmenter application in MATLAB. LSFM z-stacks were

screened in ImageJ to identify a suitable optical plane containing foreground (cells) and background (biomatrix and pores) objects for manual pre-training. Whole cell areas were labeled as foreground pixels without overlapping regions. The biomatrix, pores, and void region outside the biomatrix were labeled as background pixels. Binary output images were created and saved as TIFF files.

For deep learning cell segmentation, iLastik (version 1.4.0. post1-gpu) was run on a 64-bit Windows laptop equipped with an NVIDIA GeForce RTX 2070 GPU. The neural network module was employed, utilizing the 3D StarDist model for single cell segmentation. The 3D StarDist model was obtained pre-trained to segment individual cell nuclei from 3D volumes (not with our datasets), which was applicable to the CRLM biomatrix model, as cancer cells in our datasets exhibited comparable ovoid morphology to the pre-trained dataset. The resultant .h5 files were opened in MATLAB and binary masks were saved as TIFF files.

2.12 Statistical analysis

Statistical analysis and hypothesis testing were performed with MATLAB and Prism 10 (GraphPad Software, Boston, MA) software. All reported values represent the mean and standard error of the mean taken from 3–5 biological replicates (experimental iterations) and multiple technical replicates (individual biomatrices) per condition. DNA quantification was displayed as ng of DNA per μL of volume and normalized to tissue wet weight (mg) prior to digestion and quantification. Hydroxyproline and GAG content measurements were presented as proportions ($\mu\text{g } \mu\text{g}^{-1}$) of total protein content in each sample. Cell viability measurements from each experiment were normalized to the mean MTS assay absorbance of parallel day 0 control samples to report fold change in viability over time.

3 Results

3.1 Decellularization removes cellular content while upholding biochemical composition of liver tissue

The decellularization process for porcine liver tissues includes sectioning, water and detergent washes, DNase treatment, lyophilization, and rehydration (Fig. 1A). Decellularization efficiency was confirmed by measuring DNA content normalized to tissue weight. Fresh liver tissue sections produced $104.8 \pm 15.6 \text{ ng } \mu\text{L}^{-1} \text{ mg}^{-1}$ DNA whereas liver biomatrices measured significantly lower at $3.9 \pm 1.00 \text{ ng } \mu\text{L}^{-1} \text{ mg}^{-1}$, for a 96% reduction ($****p < 0.0001$, unpaired *t* test, Fig. 1B). A 24-hour swelling test showed decellularized biomatrices successfully retained water to increase their mass 2.64 times from their lyophilized state.

To evaluate the effects of the decellularization process on the tissue structure, biochemical composition analysis *via* Fourier transform infrared spectroscopy (FTIR; Fig. 1C), collagen and glycosaminoglycans (GAGs) quantification, and trichrome histology (Fig. 1E), was performed on representative



tissues subjected to various decellularization steps. Unprocessed fresh sections (stage 1) were compared with tissues evaluated after detergent washes (stage 2), DNase treatment (stage 3), and lyophilization and subsequent rehydration (stage 4). The FTIR spectrum of stage 1 tissue exhibited prominent peaks at approximately $3200\text{--}3400\text{ cm}^{-1}$ (amide A, N–H stretching), 2920 cm^{-1} (amide B, N–H stretching), 1631 cm^{-1} (amide I, C=O stretching), 1555 cm^{-1} (amide II, N–H bending), and 1260 cm^{-1} (amide III, C–N stretching).^{24–26} Stage 2 and 3 samples produced FTIR spectra containing similar peaks, indicating that the detergent and enzymatic treatments did not significantly affect the tissue composition. Following lyophilization and rehydration of the decellularized tissue (stage 4), the original peaks were conserved (Fig. 1C). The FTIR spectra collected from stages 1–4 resemble that of collagen,^{26,27} indicating a strong presence of collagen in fresh porcine liver tissue that is maintained throughout the decellularization process. FTIR contributions from cellular components are present but comparatively minimal to collagen within the dECM biomatrix.²⁸

With these data, and the prior knowledge that the liver is a collagen-rich environment, the maintenance of collagen through decellularization was assessed by quantification of hydroxyproline. Hydroxyproline content was $26.13 \pm 4.63\%$ of total protein within the dECM biomatrices, further indicating a high estimated collagen content upheld through decellularization (Fig. 1D). In fresh tissue where the majority presence of cells contributed to protein quantity and diversity, hydroxyproline only represented $1.79 \pm 0.08\%$ of protein ($**p < 0.01$, unpaired *t* test, Fig. 1D). GAGs were also measured and were robustly maintained within liver tissue through the decellularization process (compare $0.70 \pm 0.06\text{ }\mu\text{g GAGs per }\mu\text{g total protein}$ at stage 1 to $0.42 \pm 0.22\text{ }\mu\text{g }\mu\text{g}^{-1}$ at stage 4; ns, unpaired *t* test, Fig. 1D).

Masson's trichrome staining visually corroborated these findings. Fresh porcine liver tissue (stage 1) sections show black-stained nuclei within red cells fully surrounding intact blue collagen fiber bundles (Fig. 1E). Successful decellularization was confirmed by a majority loss of black and red-stained structures by stage 2. Residual cellular material was cleared by stage 3 and collagen presence and structure was maintained through all 4 stages. Following lyophilization and rehydration (stage 4), qualitative assessment of the trichrome staining suggests that the collagen pores were maintained while collagen fiber bundles were slightly more concentrated than those of earlier stages.

3.2 Optical clearing protocols enhanced imaging depth and contrast in dECM biomatrices

Optical clearing can improve imaging depth by reducing light scattering within tissues. Here, the improvement in light sheet fluorescence microscopy (LSFM) imaging depth was compared between an uncleared biomatrix and biomatrices cleared with refractive index matching solution (RIMS) or iDISCO+/EC protocols (Fig. 2). To evaluate the improvement in image contrast after optical clearing, representative LSFM images of collagen

autofluorescence were qualitatively compared, and an intensity profile line along a central image slice from each dataset was quantified, as the central image slice corresponds to the deepest plane and most challenging-to-image region of the biomatrix relative to the microscope objective lenses. Uncleared biomatrices did not permit LSFM illumination nor visualization of the interior architecture (Fig. 2A). The fluorescence intensity along the central slice decreased rapidly with depth (Fig. 2B), with resolvable intensity peaks detected only within approximately $437\text{ }\mu\text{m}$ of the tissue surface. The first derivative of the intensity profile highlights sharp intensity changes, effectively localizing object and structure boundaries. Higher absolute values of the first derivative of the intensity line profile signify higher image contrast (resolvable signal), which is necessary to resolve and segment separate objects, such as collagen pores. The first derivative of the intensity line profile of the uncleared tissue decreased at a distance of $437\text{ }\mu\text{m}$ from the biomatrix surface, indicating the loss of high contrast and resolvable signal beginning at this depth (Fig. 2C).

The Nycodenz-based RIMS clearing protocol¹ improved LSFM imaging depth within the biomatrix compared to uncleared biomatrices. Greater signal and contrast were visibly apparent in the representative central slice image (Fig. 2D) and in the intensity profile (Fig. 2E). However, LSFM of the RIMS-cleared biomatrix only achieved visualization within approximately 2 mm below the biomatrix surface. A sharp drop in contrast was observed in the first derivative curve of the line profile of RIMS-cleared biomatrices at an interior depth of $2035\text{ }\mu\text{m}$ (Fig. 2F).

The optimized iDISCO+/EC protocol permitted high-fidelity visualization of the entire biomatrix structure in 3D. Even at the depth of the center slice of the image stack, there was sufficient signal and contrast to identify the porous dECM architecture (Fig. 2G). The intensity profile showed minimal loss of resolution or contrast throughout the volume (Fig. 2H). High image contrast was also preserved throughout the thickness of the biomatrix, evident by the derivative curve maintaining large and sharp peaks throughout the $>3\text{ mm}$ cross section (Fig. 2I). Furthermore, the full dynamic range of the camera could be used following this optimized clearing protocol, whereas uncleared and RIMS-cleared samples only used a fraction of the range even with higher illumination power and longer camera integration times. The optimized iDISCO+/EC clearing protocol permitted the acquisition of high spatial resolution data ($<2^3\text{ }\mu\text{m}^3$ isotropic voxels), which is critical for quantification of dECM porosity and cell invasion in 3D with cellular-level resolution throughout millimeter-sized (mesoscopic) samples. These results motivated future use of the iDISCO+/EC clearing protocol for whole-volume, mesoscopic, 3D imaging of fluorescent structures in complex dECM models.

3.3 Bioengineered colorectal cancer liver metastases were established within the dECM liver

A workflow schematic for engineering colorectal cancer liver metastases (CRLM) within dECM liver biomatrices is shown in



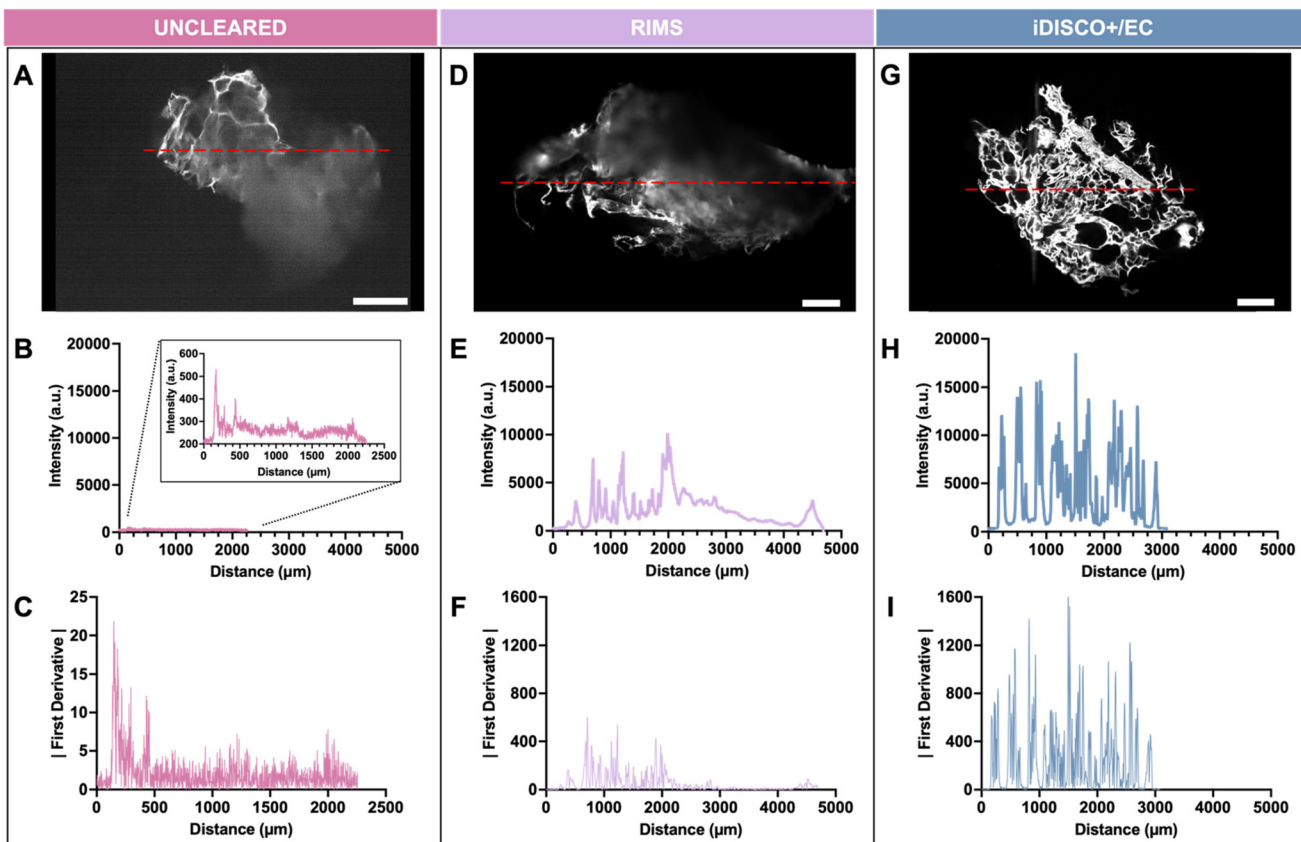


Fig. 2 Optical clearance methods for dECM visualization. (A) The central slice from an LSFM image stack of a representative uncleared biomatrix shows rapid loss of signal and contrast with depth. The red line indicates an arbitrary path along which signal intensity was calculated through the thickness of the sample. (B) The intensity profile shows that, without clearing, visualization is limited to only ~ 400 μm into the biomatrix. (C) The absolute value of the first derivative vector of the intensity profile further demonstrates this limitation as contrast peaks are significantly reduced around 437 μm . (D) The light sheet image of a RIMS-cleared sample suggests increased intensity compared to uncleared samples, which is confirmed by the corresponding intensity profile (E) with signal depth increased to ~ 2 mm and (F) derivative contrast peaks maintained to 2035 μm . (G) Increased overall signal and contrast is evident in iDISCO+/EC prepared samples as seen in the representative central image slice. (H) The optimized clearing protocol enabled the deepest (>3 mm) visualization into the biomatrix with the most well-maintained signal intensity. (I) This method also produced the largest and sharpest derivative peaks quantitatively confirming the visually apparent improvement in contrast. Scale bars = 500 μm .

Fig. 3A. Once colorectal cancer spheroids were fully formed on hanging drop array plates, they were seeded onto prepared dECM liver biomatrices and allowed to colonize and grow for 3 days. Following seeding and initial colonization, cell-seeded biomatrices were either maintained as untreated controls or treated with oxaliplatin for another 2 days (Fig. 3A). Oxaliplatin treatment was used to demonstrate the capability of optical imaging to delineate differences in metastatic colonies upon drug treatment in recellularized dECM.

To visualize the colonization per established standards,¹ we first utilized scanning electron microscopy (SEM) and the MTS viability assay. Scanning electron micrographs visually confirmed colonization of the liver scaffolds by day 3, as is evident by cells occupying the dECM biomatrix (Fig. 3B). SEM images show increased cellular occupancy by day 5 in control, untreated biomatrices (Fig. 3C) and a significant reduction in the number of adhered cells with oxaliplatin treatment (Fig. 3D). An orthogonal, non-visual confirmation of cell proliferation and death

was performed using the MTS assay in which changes in viability measurements across timepoints or conditions indicate population growth or death (Fig. 3E). CRLM viability increased 2.66 ± 0.29 -fold to show proliferation from day 0 to day 3 ($^{***}p < 0.0001$, two-way ANOVA) which continued through day 5 (4.59 ± 0.34 -fold increase from day 0; $^{***}p < 0.0001$, two-way ANOVA). Oxaliplatin successfully induced cell death evidenced by an approximately 41% reduction in viability across the 48-hour treatment time (day 3 to day 5; $^{**}p < 0.01$, two-way ANOVA) and a remaining population 66% smaller than parallel untreated controls at that same timepoint (day 5 control vs. day 5 oxaliplatin; $^{***}p < 0.0001$, two-way ANOVA).

3.4 LSFM permitted high-resolution full volume imaging of heterogenous dECM biomatrix structures

We evaluated 3 optical fluorescence microscopy methods, wide-field, confocal, and light sheet, to excite collagen autofluorescence and visualize the interior of the biomatrices



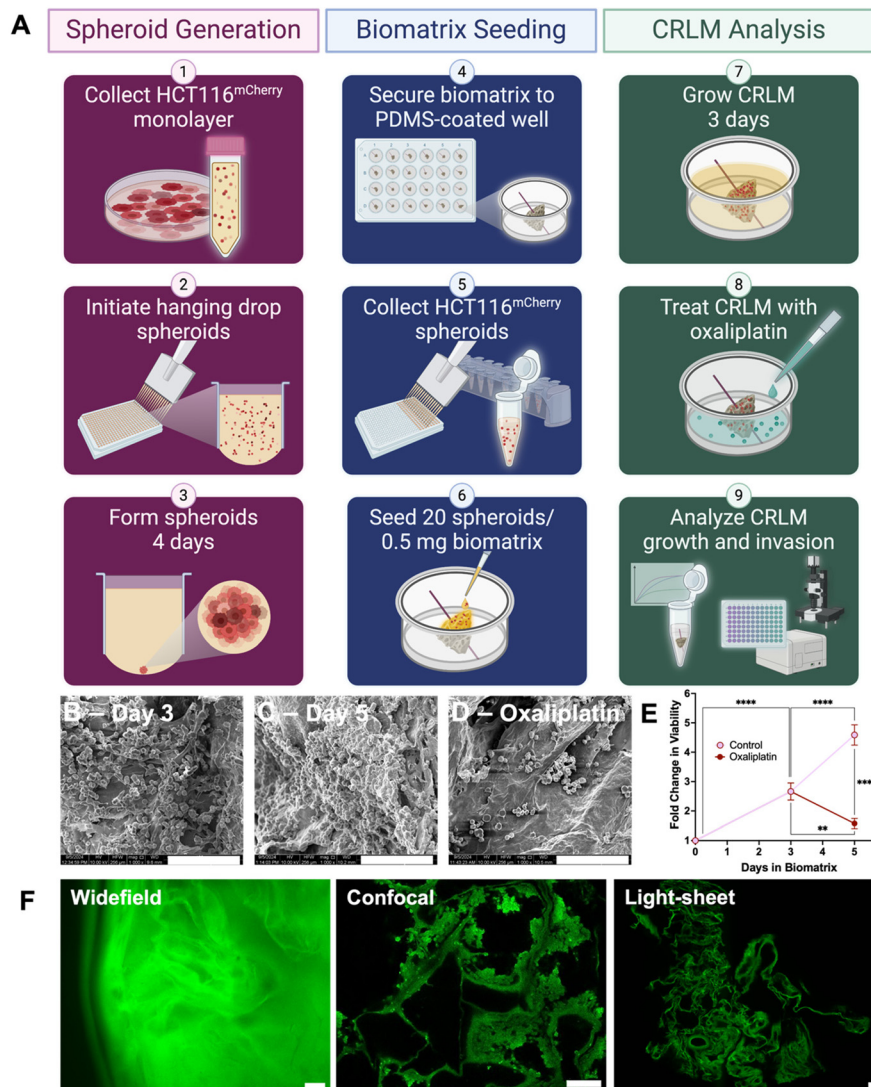


(Fig. 3F). Day 3 CRLM samples were fixed and cleared with the optimized iDISCO+/EC protocol. Widefield fluorescence microscopy did not permit visualization of the biomatrix interior or architecture (Fig. 3F, left). Confocal microscopy permitted imaging deep into the biomatrix with high spatial resolution (<1 μ m; Fig. 3F, middle). LSFM was able to image the entire 3D biomatrix volume with moderate spatial resolution (<2 μ m; Fig. 3F, right). Despite the increased resolution achieved by confocal imaging, it has a limited imaging depth (500 μ m), and

slow speed (hours) as compared to LSFM which can achieve greater depth in a shorter time (seconds to minutes). LSFM was applied for future imaging of 3D volumes for quantification of dECM biomatrix porosity and cellular invasion.

3.5 Automated segmentation and analysis of dECM biomatrix porosity following LSFM

Due to the importance of biomatrix porosity in cell recolonization and lack of quantitative porosity assays, we developed an

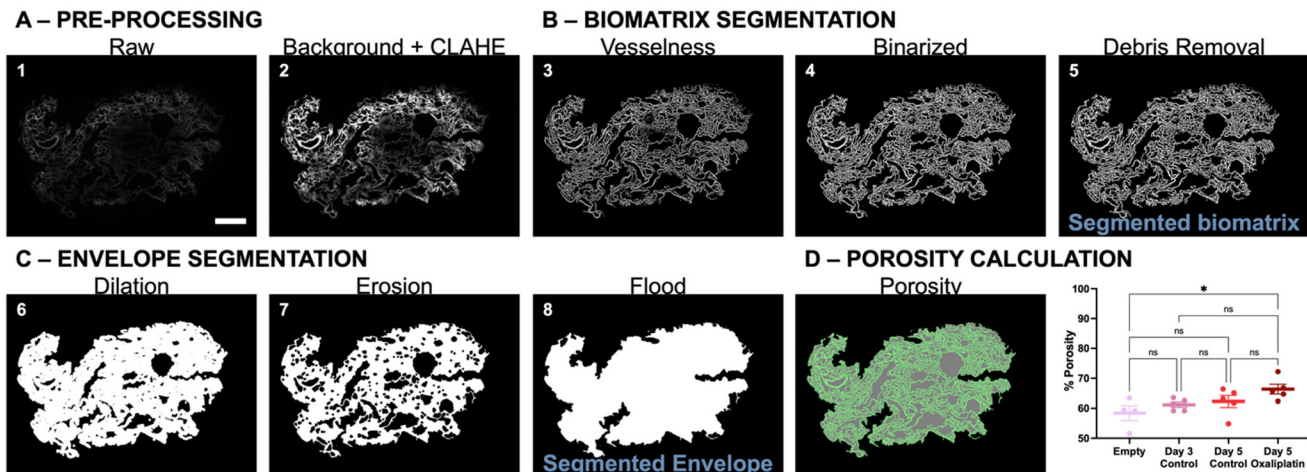


Fig. 4 Workflow for dECM image processing and segmentation. A representative LSFM image slice from one liver biomatrix is used to demonstrate the procedure for segmenting the biomatrix structure. (A) Biomatrix porous architecture is visible in raw cross-sectional images (A1). Images were pre-processed to improve contrast with a 50-pixel background subtraction and 20-pixel CLAHE filter (A2). (B) Matrix segmentation was achieved by first applying a 10-pixel Frangi vesselness filter to enhance ridge-like features (B3). The volumes were then binarized using a high-pass filter (threshold = 0.1; B4) and small disconnected objects (debris) were removed using a second high-pass filter (threshold = 150 voxels; B5). (C) The entire biomatrix envelope (convex hull) was then segmented by 9-pixel dilation (C6) and erosion (C7) followed by a flood fill (C8). Scale bar = 500 μ m. (D) Overlaying the segmented biomatrix (B5) with the segmented envelope (C8) provides a visual representation of how porosity was quantified per slice using eqn (1). This per-slice porosity value was then scaled by pixel volume to generate full-volume 3D porosity values. Average porosity across all conditions was 62.04%, with no change between the empty biomatrix and any recellularized CRLM conditions other than a slight increase observed in day 5 oxaliplatin-treated samples (* $p < 0.05$, one-way ANOVA).

advanced image analysis protocol to identify the collected biomatrix autofluorescence signal and quantify matrix porosity from LSFM volumetric images of the dECM models (Fig. 4). The processing steps are shown for a representative LSFM image slice (Fig. 4A–C). First, LSFM image sections were stitched together into a volume within Imaris and converted to TIFF files for downstream processing in ImageJ (Fig. 4A1). A 50-pixel local background subtraction and a 20-pixel contrast-limited adaptive histogram equalization (CLAHE) filter were applied to remove background fluorescent signal and increase ECM signal contrast for deep planes within the biomatrix (Fig. 4A2).²⁹ Next, a 10-pixel Frangi vesselness filter was used to enhance vessel, tubular, and ridge-like spatial features (Fig. 4B3).³⁰ Volumes were then binarized using a high-pass filter (threshold = 0.1, Fig. 4B4) and a second high-pass filter (threshold = 150 voxels) removed small objects such as cells and debris from the binarized volume. The result was used as the 3D volume, accounting for voxels occupied by the dECM biomatrix structure (Fig. 4B5).

To calculate porosity, the entire biomatrix envelope volume needed to be calculated, as well. To do this, 9-pixel dilation (Fig. 4C6) was followed by 9-pixel erosion (Fig. 4C7), and a flood-fill (Fig. 4C8) operation was sequentially performed on each 2D image slice of the binarized biomatrix volume. The biomatrix and envelope volumes were quantified as the sum of voxels scaled by the voxel spatial dimensions. Biomatrix volume was subtracted from the envelope volume using eqn (1) to calculate a porosity measurement for each sample (Fig. 4D). The mean quantified porosity of the biomatrices was

similar across all conditions ($58.4 \pm 4.3\%$, $61.3 \pm 1.8\%$, $62.3 \pm 4.1\%$, and $66.3 \pm 3.3\%$ for empty, day 3 control, day 5 control, and day 5 oxaliplatin-treated samples, respectively; Fig. 4D) and only showed a slight increase in the oxaliplatin-treated samples compared to empty biomatrices (* $p < 0.05$, one-way ANOVA). The 95% confidence interval for biomatrix porosity quantified from LSFM data ($n = 19$) was 60.2–64.3%. These results illustrate reproducibility of this characteristic of our dECM biomatrices, not only before, but throughout CRLM culture, which is critical for well-controlled studies of cell–ECM interactions.

3.6 Customized cell labeling protocols validate high contrast visualization of deeply embedded cancer cells in dECM biomatrices

After cell seeding and subsequent culture of the CRLM samples, the biomatrices were fixed, cleared and imaged using the optimized iDISCO+/EC and LSFM protocols. However, localization of individual mCherry⁺ colorectal cancer cells within the biomatrix was difficult, likely due to reduction in cellular immunofluorescence due to the clearing protocol.³¹ Whereas some cells produced very bright mCherry fluorescence, other areas were dim (Fig. 5A and B). Furthermore, Z-stack flythroughs of the 3D reconstruction of the biomatrix show bright, small, circular fluorescent spots that were attributed to lipofuscin deposits (Video S1). A representative slice containing a metastatic nest burrowed in a porous region of interest (ROI) demonstrates the visualization limitations, as only one large bright spot is visible within the pore (Fig. 5C).



The spot's fluorescent signal is easily distinguishable from the ECM architecture by both visual observation and automated cell segmentation (Fig. 5D and E). Two arbitrary path lines were drawn on the image slice along which signal intensity was measured to show a singular peak in signal corresponding with that one bright spot (Fig. 5F, top). This spot, measuring around 25 μm in diameter, was decidedly too large to represent a singular or precisely segmented cell, suggesting the mCherry reporter was limiting the ability to properly identify individual cells.

For improved visualization and segmentation, the cells were additionally dyed with BioTracker, a cytoplasmic membrane dye, which was compared with mCherry. The BioTracker dye uniformly labeled the cells throughout the biomatrix as seen in the representative 3D reconstruction and Z-stack flythrough (Video S2), as well as in the volume projections (Fig. 5G and H). The same image slice and ROI was analyzed for direct comparison of cellular identification. Imaging with the BioTracker stain revealed the presence of multiple cells within the metastatic nest, identified by distinct spots $<20 \mu\text{m}$ in diameter (Fig. 5I) which were also successfully segmented (Fig. 5J and K) and produced definite peaks in the intensity profiles (Fig. 5F, bottom). BioTracker labeling efficiency was confirmed with additional DAPI staining which mirrored the presence of stained spherical structures nestled throughout the biomatrix (Video S3). BioTracker labeled the same spherical structures as DAPI (Fig. S1A-C) and resulted in improved visualization and contrast over DAPI within the biomatrix (Fig. S1C-E and Video

S4). These data motivated the use of the BioTracker dye for future analysis of cell-seeded biomatrices.

3.7 Custom image analysis pipeline enables significantly improved segmentation of cells, outperforming current analysis methods

Once adequate cellular labeling was established, a custom image analysis algorithm was constructed to process the cellular data in the context of the 3D dECM volume and extract relevant quantifiable biological information like occupation and invasion. Our analysis procedure for segmenting BioTracker-labeled cells throughout the biomatrix was optimized and performed in ImageJ using the Imaris-stitched volumes previously described (see section 3.4). Raw stitched cross-sectional image slices require pre-processing for accurate cell segmentation, and visualization of the effects of each processing step is provided for a representative image (Fig. 6A). First, a 10-pixel CLAHE filter was applied to enhance contrast of the cells, followed by a 3-pixel local background subtraction, and a 3×3 sharpening filter to highlight round objects. Then, the fast Fourier transform (FFT) of each 2D plane was acquired and high-pass filtered with a $24.29 \mu\text{m}$ per cycle cut-off frequency to isolate small objects. The inverse FFT was taken and automatically binarized using the IsoData algorithm and a 3D watershed was used to separate touching objects. The final cell segmentation step was performed in Imaris using the 'spot' function to segment circular or cell-like structures with an estimated $8 \mu\text{m}$ diameter (Fig. 6A). This diameter was chosen after

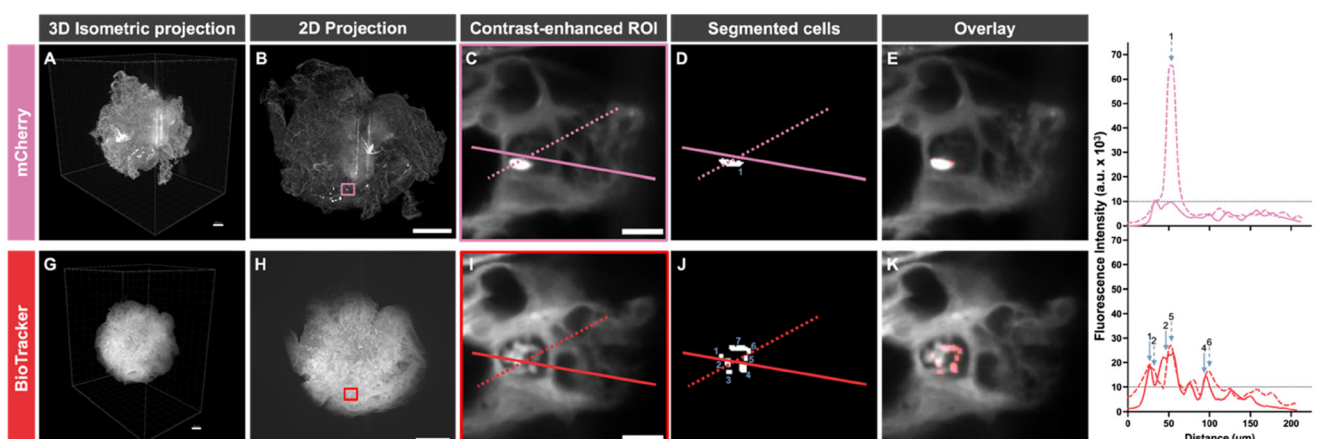


Fig. 5 Optimizing cellular visualization with fluorescent reporters. A representative biomatrix recellularized with mCherry⁺ colorectal cancer cells before (A–E) and after (G–K) 655 nm BioTracker cytoplasmic membrane dye staining. (A) A 3D isometric projection of an mCherry⁺ cell-seeded biomatrix and its corresponding 2D maximum intensity projection (B) demonstrate the nonuniform expression of mCherry fluorescent signal. Small ($<4 \mu\text{m}$), circular fluorescent spots, presumably lipofuscin, are apparent throughout the biomatrix. (C) A porous ROI (pink box) containing mCherry signal was chosen to compare cell identification methods. A single bright, elliptical-shaped, and relatively large (25 μm diameter) object is visible and detected by cell segmentation (D and E). Pink lines were arbitrarily drawn across the image slice along which fluorescence intensity profiles were plotted. (F) The fluorescence intensity profiles along the solid and dashed lines show one singular peak visible at the point where the dashed line intersects the single identified "cell". (G) CRLM samples were stained with the 655 nm BioTracker cytoplasmic membrane dye and representative 3D and (H) 2D projections show more uniform distribution of cellular fluorescent signal throughout the biomatrix as compared to the transgenic mCherry fluorescent label. The background fluorescence from the dECM was also more uniform, without the spots attributed to lipofuscin deposits. (I) The same ROI (red box) is shown where 7 cells are now identified by segmentation after BioTracker labeling (J and K). These successfully segmented cells correspond to peaks in the intensity profile (F, bottom) to show how BioTracker provides improved visualization and resolution of cells from the biomatrix. 3D projection scale bars = 200 μm . 2D projection scale bars = 500 μm . ROI scale bars = 50 μm .



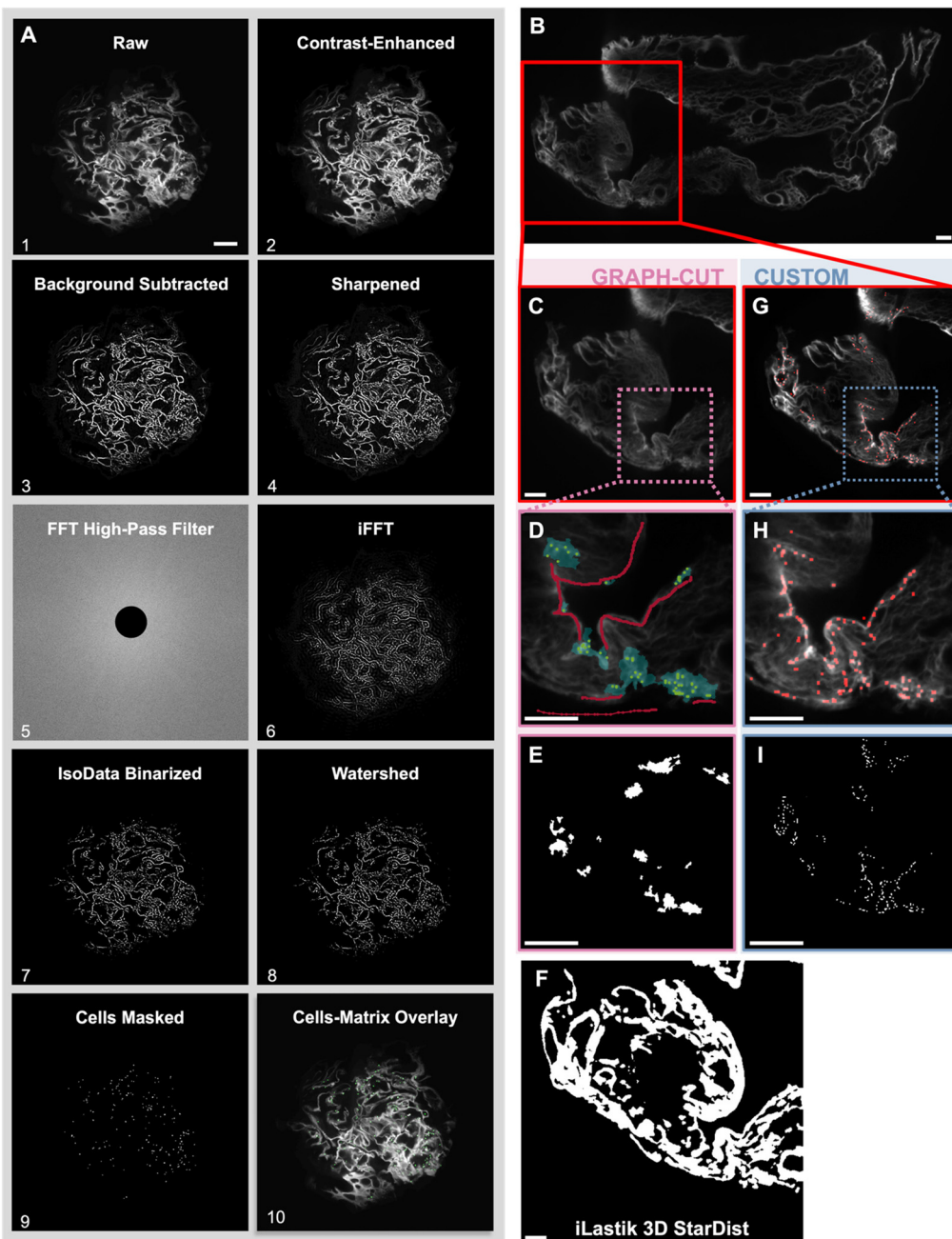


Fig. 6 Custom image processing procedure for segmentation of colorectal cancer cells from the biomatrix performs better than current methods. (A) A representative stitched LSFM image slice is shown to demonstrate the steps taken to process LSFM volumes. Cells are visible in the raw image (1) but required pre-processing using a 10-pixel CLAHE filter (2) for contrast enhancement, a 3-pixel sliding background subtraction (3), and image sharpening (4) to be properly segmented. Then, the FFT and a high-pass filter ($\omega_c = 24.29 \mu\text{m}$ per cycle) were applied (5). The inverse FFT was taken (6), and the result binarized using IsoData thresholding (7). A 3D watershed was used to separate touching objects in the binarized 3D volume (8). Cells were identified in Imaris by size (threshold = 8 μm) and masked (9). A representative image overlay identifies cells (green) within the biomatrix (10). Scale bar = 200 μm . (B) A representative LSFM image slice of BioTracker-labeled cells within the biomatrix was chosen to compare the Graph-cut image segmentation method to custom algorithms and show the insufficiency of Graph-cut. Scale bar = 100 μm . Graph-cut requires the user to first screen the 3D dataset to identify (C) a 2D ROI that contains both foreground and background objects. (D) Within that ROI, the user must then manually label foreground (light green) and background (red boundary) pixels, to which Graph-cut applies graph theory for segmentation. The segmentation output is correspondingly shown by the teal shaded regions and (E) binary mask. This method resulted in low-resolution segmentation of the foreground (cells), failing to identify individual cells as is needed for 3D cell invasion analysis. Scale bars = 100 μm . (F) Without manual pre-training specific to our dataset, the 3D StarDist iLastik deep learning algorithm was similarly unable to segment individual cells, additionally including large sections of ECM wrongly in the cell segmentation. Scale bar = 100 μm . (G) The same 2D ROI was used to demonstrate improved segmentation of BioTracker-labeled cancer cells (red) using the custom algorithm developed in this publication. Scale bar = 100 μm . (H) Red spots within the ROI represent cells identified within the biomatrix and appear as distinct points rather than large nests. (I) A representative 2D slice output of the binary cell segmentation. Scale bars = 100 μm .



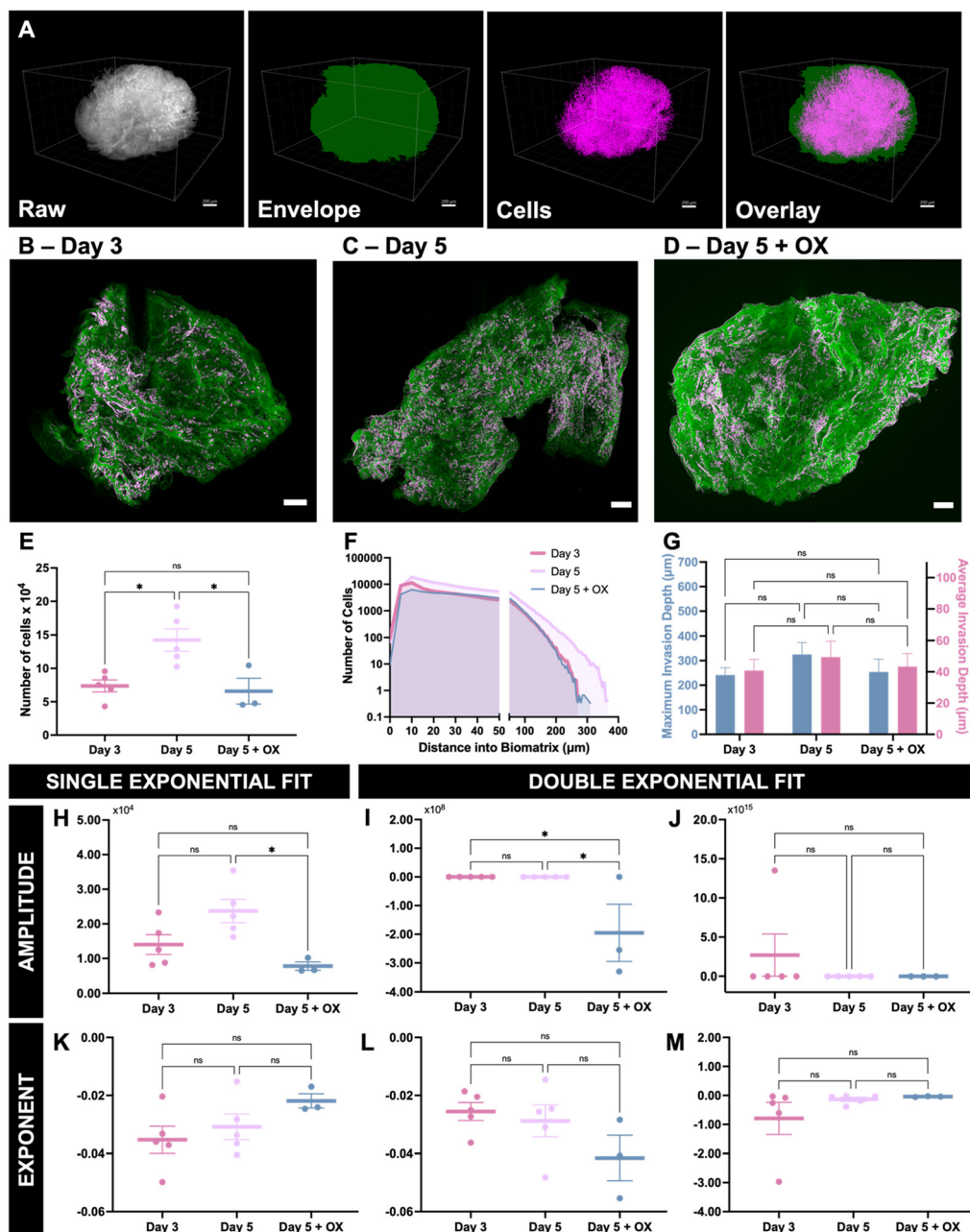


Fig. 7 Analysis of colorectal cancer cell invasion of liver biomatrices. Colorectal cancer cells were cultured on liver biomatrices to establish *in vitro* CRLM. Samples were fixed and processed with the newly optimized protocols and imaged with LSFM for invasion analysis. (A) A visual summary of the process of quantifying cellular invasion into biomatrix volumes is shown by representative Imaris 3D isometric views of the raw biomatrix LSFM volume, the segmented biomatrix envelope, segmented cells, and the cell/envelope overlay. A distance transformation performed on the final overlaid data set quantifies the shortest distance from every cell to the outside of the biomatrix envelope as invasion depth. Scale bars = 200 μ m. (B) A representative overlay of a recellularized biomatrix on day 3 provides another example of segmented biomatrices (green) and their colonized cells (pink) within 3D volumes. Representative day 5 control (C) and oxaliplatin-treated (D) samples are also shown. Scale bars = 250 μ m. (E) The total number of cells detected in day 5 control samples was significantly higher than day 3 (compare $7.39 \pm 0.89 \times 10^4$ cells at day 3 to $14.24 \pm 1.68 \times 10^4$ cells by day 5; * $p < 0.05$, one-way ANOVA), further demonstrating cellular proliferation within the dECM biomatrices. This cell number was reduced when oxaliplatin was used to control the population (* $p < 0.05$, one-way ANOVA). (F) The distributions of the number of cells detected plotted as a function of the distance from the biomatrix surface at which they were found, shows increased invasion depth in day 5 control samples compared to day 3 (**** $p < 0.01$, Kolmogorov–Smirnov). Invasion depth was also significantly restricted by oxaliplatin treatment compared to day 5 control samples (* $p < 0.01$, Kolmogorov–Smirnov). (G) These changes in maximum invasion depth, along with average cell invasion depth, though visually evident, are not significantly different from each other across conditions (ns, two-way ANOVA). Single and double exponential fits were applied to the cell invasion distributions (averaged in C) and average amplitude for the single (H) and double (I and J) fits are reported and compared to show a decrease in the amplitude between day 5 control and oxaliplatin-treated samples for the single exponential and the first amplitude term for the double exponential fit (* $p < 0.05$, one-way ANOVA). No significant changes were observed in the exponent terms of either the single (K) or double (L and M) exponential fits.

empirically measuring the diameter of BioTracker-labeled cells in the raw LSFM volumes.

For comparison, the well-established Graph-cut image analysis method was also applied to segment cancer cells from the liver ECM in a representative image slice (Fig. 6B). This process involved manual pre-training to identify foreground pixels (cells) and background pixels (dECM and void space) as shown in Fig. 6D. The resulting binary segmentation in Fig. 6E reveals large low-resolution areas identified by the algorithm as cells, even with the direct pixel identification inputs for cell-laden foreground regions. The binary segmentation produced by the iLastik method similarly shows areas too large to be individual cells as well as large portions of the biomatrix itself segmented in error as cells (Fig. 6F). Both segmentations appear in stark contrast to the custom analysis method which, in the same ROI (Fig. 6G), identifies spots without manual training (Fig. 6H) to produce a much higher resolution binary segmentation which displays individual cells as opposed to cell clusters (Fig. 6I). As such, Graph-cut and iLastik both sub-optimally segmented cells. iLastik specifically included much of the biomatrix, including vasculature, in the cell classification and both methods displayed merged cell regions, rendering them incapable of delineating individual cells for accurate quantification of cell number and invasion.

3.8 Integrated imaging and analysis pipeline quantified cellular processes within the engineered dECM-based CRLM model

To quantify 3D cellular invasion of the biomatrix, the segmented cells and biomatrix envelope 3D volumes were combined in ImageJ as a single 4D multi-channel dataset (Fig. 7A). This 4D dataset was analyzed with Imaris. First, the 'surface' function was used to generate a 3D rendering of the biomatrix envelope to serve as the starting surface (*i.e.* depth = 0 μm) from which to measure cell invasion into the biomatrix. Since the biomatrix envelope data was already binarized for porosity calculations (Fig. 4C8), simple high-pass intensity and voxel thresholds were applied to achieve 3D surface generation (Fig. 7A). The cell spot renderings were then created using the Imaris 'spot' function and a high-pass filter (Fig. 6). The data was then converted to 32-bit float. Finally, a distance transformation was performed to measure the shortest distance for each cell to the outside of the biomatrix envelope.

Using this custom image analysis methodology, the effects of time and the chemotherapy drug oxaliplatin on the metastatic colorectal cancer cellular invasion of the biomatrices were quantified. Cells were visible along the outer surface of all biomatrices analyzed, with decreasing cell number observed with increasing biomatrix depth. Representative image overlays of the biomatrix and detected cells illustrate the colonization and proliferation of cells from day 3 (Fig. 7B) to day 5 (Fig. 7C), and the effects of oxaliplatin treatment on proliferation (Fig. 7D).

LSFM combined with quantitative image analysis allowed enumeration of cells within the biomatrix and quantification of invasion distance. The number of cells detected within day

5 control biomatrices was 1.93 times higher than day 3 ($*p < 0.05$, one-way ANOVA; Fig. 7E). Death by oxaliplatin was detectable with our image and analysis methods as evidenced by a 56% reduction in cell number in oxaliplatin-treated samples compared to day 5 controls ($*p < 0.05$, one-way ANOVA; Fig. 7E). The cell invasion distribution for each biomatrix sample was used to calculate the average biomatrix cell invasion distribution for each condition. Day 5 control cells were found at slightly increased depth within the biomatrix compared to day 3 control and day 5 oxaliplatin-treated samples (maximum and average invasion depth; ns, two-way ANOVA; Fig. 7F and G). The average depth of invasion for cells by day 3 was $40.80 \pm 3.22 \mu\text{m}$ with an average maximum invasion depth per sample of $241.40 \pm 13.33 \mu\text{m}$. These values increased with time to an average depth of $49.40 \pm 4.56 \mu\text{m}$ and average maximum depth reached in each sample of $325.00 \pm 21.76 \mu\text{m}$ by day 5. Oxaliplatin-treated samples demonstrated a slight reduction in invasion as compared to day 5 control samples, with an average invasion depth of $43.33 \pm 4.84 \mu\text{m}$ and average maximum invasion depth of $254.00 \pm 30.09 \mu\text{m}$. Using a Kolmogorov-Smirnov test, statistically significant differences in the mean cell invasion distributions were found between day 3 and day 5 ($****p < 0.00005$), and day 5 control and oxaliplatin-treated conditions ($*p < 0.05$; Fig. 7F). These findings emphasize the dynamic nature of metastasis within dECM tissue models and highlight our platform's ability to quantitatively monitor treatment effects over time.

Mathematical modeling of complex, dynamic processes like metastasis, cellular invasion, or migration could enable a more detailed understanding of these phenomena by breaking them down into quantifiable and potentially controllable components.³² Here, single and double exponential fits were applied to the cell invasion distribution for each biomatrix (averaged distributions shown in Fig. 7F), and average exponential fits were calculated for each condition. The exponential terms for the single and double exponential fits did not show statistical significance (Fig. 7K-M). Significant differences were found for the amplitude term for the single exponential (Fig. 7H) and first amplitude term for the double exponential fit (Fig. 7I) between day 5 control and oxaliplatin-treated samples ($*p < 0.05$, one-way ANOVA). These findings suggest that oxaliplatin treatment affects the scale of cellular invasion rather than the rate, indicating an inhibitory effect on CRLM within the dECM biomatrix model. Further, these findings illustrate that dECM models can effectively mimic metastatic behavior and therapeutic response and could aid in screening and identifying anti-metastatic drugs with the help of our new analysis pipeline.

4 Discussion

The advancement of new, 3D biomimetic systems necessitates corresponding development of novel analytical tools. Decellularized extracellular matrix (dECM) scaffolds offer a widely adaptable *in vitro* platform to analyze the effects of 3D



tissue-specific environments on cellular processes. However, there are limited high-resolution methods available to analyze complex models like recellularized dECM without compromising spatial information. dECM scaffolds are defined by their inherent complexity, heterogeneity, thickness and opacity.^{1,33-36} Therefore, extracting spatially relevant information, whether from the biomaterial itself, or cell-biomaterial interactions therein, requires unique optimization of sample preparation and imaging, as well as material characterization and analysis methods. This work presents new, optimized optical imaging and analysis tools which enable two powerful sets of spatially relevant analytics: (1) visualization of dECM scaffolds to extract scaffold architecture and structural information; and (2) cell-biomaterial visualization and behavioral analysis within repopulated dECM scaffolds.

As a use case for our imaging and automated analytics methods, we demonstrated their capability within engineered colorectal cancer liver metastasis (CRLM) models. Our work began by characterizing the dECM biomatrix alone, using classical methods rooted in biomaterials science. Successful decellularization was verified *via* quantification of residual DNA following decellularization protocols.³⁷⁻³⁹ Preservation of collagen and GAG content was evaluated in several ways, including hydroxyproline and GAG assays,³⁸⁻⁴⁰ trichrome staining^{37,41} and Fourier transform infrared spectroscopy (FTIR).^{42,43} The dECM liver biomatrix FTIR spectra confirmed results from parallel scaffold characterization techniques to demonstrate that the collagen fibers and molecular bonds of the ECM were preserved through each stage of the decellularization process evidenced by amide bands A, B, I, II and II (Fig. 1C).^{26,27}

Imaging methods are of particular interest in the analysis of dECM-based models because of the opportunity to retain spatial context. However, the large size of our dECM biomatrices ($\sim 2 \times 2 \times 2$ mm) and required cell-level resolution present challenges for microscopy. While scanning electron microscopy (SEM) can visualize tissue architecture (Fig. 3B-D),^{1,44} and has much higher spatial resolution (nm) than optical microscopy techniques (μm), the nanoscopic imaging volume makes it tedious for studying 3D cellular invasion. Confocal microscopy demonstrated sufficient resolution to visualize 3D cell distribution on biomatrices (Fig. 3F), but is limited by accessible depth. Light sheet fluorescence microscopy (LSFM) permits large volume image acquisition through decoupled illumination and detection paths with relatively long (>2 mm) working distance objective lenses. LSFM has the additional benefit of imaging speed to make acquiring large data sets feasible. For example, it takes approximately 34 seconds to image a $3 \times 3 \times 3$ mm³ biomatrix with optimized parameters ($1.79^3 \mu\text{m}^3$ voxels, 20 ms per frame integration time). Using the same pixel size and a 10 μs pixel dwell time, it would take a confocal microscope approximately 13 hours to image the same biomatrix. Therefore, LSFM is uniquely appropriate to acquire high-resolution 3D volumes of colorectal cancer cell-laden biomatrices in a reasonable amount of time.

dECM-based scaffolds additionally limit deep tissue imaging due to their opacity causing light scattering and absorption. Therefore, sample preparation methods require optimization of tissue clearing protocols to achieve cell-level resolution needed for whole-volume segmentation. When coupled with LSFM, tissue clearing allows high-resolution and rapid imaging of the collagen structures of dECM biomatrices (Fig. 2), since clearing stripped sources of scattering like lipids and aqueous boundaries to achieve optical transparency. High levels of scattering can still be observed in widefield images of optically clear biomatrices (Fig. 3F), as widefield microscopy lacks optical sectioning to discriminate signals from varied depths within a 3D volume.¹² In contrast, LSFM achieves optical sectioning by focusing the excitation light into a plane and has been leveraged to image entire murine organs and bodies with single-cell resolution,^{45,46} as long as those specimens are optically cleared.⁴⁷ In our previous work, a Nycodenz-based refractive index matching solution (RIMS) was used to adjust and homogenize the refractive index of the fixed tissue samples toward that of the oil imaging medium for a multiphoton microscopy (MPM) objective lens.¹ A limited maximum imaging depth of 100 μm drove the need for a more thorough method of optical clearance to achieve biologically relevant imaging depths and cellular resolution. Here, an optimized iDISCO+ protocol produced optically clear samples. Index matching of the biomatrix with ethyl cinnamate (EC) during imaging provided a drastic improvement in imaging depth and allowed visualization of cells throughout the entire biomatrix volume ($>2 \times 2 \times 2$ mm³; Fig. 2G-I). However, the clearing protocol reduced the brightness of the endogenous mCherry reporter, causing inconsistent and dim signals and necessitating additional cell labeling with BioTracker dye for greater contrast between the cells and the biomatrix (Fig. 5). BioTracker labeling specificity was validated by additional staining with DAPI. Greater scattering and tissue autofluorescence cause DAPI-labeled images of the interior of the biomatrix to appear blurry and opaque (Fig. S1 and Videos S3, S4). In fact, a previous evaluation of optical properties of porcine liver tissues found a greater absorption coefficient, greater scattering coefficient, and lower optical penetration depth with 405 nm excitation (corresponding to DAPI), compared to 655 nm (corresponding to BioTracker) excitation.⁴⁸ These results led us to conclude that BioTracker labeling enabled improved cell segmentation over DAPI staining.

Even with higher resolution and larger volume datasets, discerning key differences in dECM architecture or cellular behavior is currently limited by the inability to accurately and efficiently process those datasets. Current image segmentation methods like Graph-cut, a robust geometry-based algorithm routinely used for automated cell segmentation,⁴⁹⁻⁵² and iLastik, a deep learning pixel classifier segmentation algorithm,⁵³ failed to accurately segment cells from within the biomatrices using contrast-enhanced and raw LSFM volumes (Fig. 6)⁵⁴⁻⁵⁶ in part, due to the high autofluorescent background which marks liver dECM. Biomatrix shape and location of labeled cells within the dECM are also likely contributors,



both heterogenous compared to known or controllable systems like hydrogels. Graph-cut and iLastik also require significant amounts of time and user inputs. Despite manual labeling of foreground and background pixels in each image, Graph-cut still struggled to differentiate cells from the surrounding biomatrix, likely due to the heterogenous background (biomatrix and void space) throughout the image. iLastik is, in contrast, a machine learning tool, previously used to successfully segment neurons from whole-brain LSFM datasets.⁵³ Within iLastik, we applied the 3D StarDist cell nuclei segmentation model,⁵⁷⁻⁵⁹ but it under-segmented cells (Fig. 6F). Better results could potentially be obtained by training our own StarDist model. However, this, too, would require significant user time and effort, and be less broadly applicable to diverse dECM models.

Thus, a custom image analysis pipeline was necessary to segment the biomatrix architecture and the cells from the LSFM data accurately and efficiently, to quantify matrix porosity (Fig. 4) and identify cell locations (Fig. 6). Our algorithms relied on a combination of established image processing methods to enhance image contrast and extract meaningful quantitative readouts. First, we used a series of contrast enhancement functions to account for nonuniform biomatrix architecture producing heterogeneous background, especially deep within the image stack. Local background subtraction, sharpening, and histogram equalization²⁹ were effective to enhance details in low-contrast image regions, which proved useful for identifying cells from deep within dECM biomatrices. To amplify the matrix architecture, we creatively applied a Frangi vesselness filter³⁰ which identified the dECM's vessel-like structures. To complement this and amplify cell boundaries, we then used a fast Fourier transform (FFT) filter.^{60,61} In our previous work, spheroid-cultured clusters of colorectal cancer cells initially disaggregated upon seeding onto the biomatrix, adhering to the ECM as single cells prior to invading. With this knowledge, the 8 μm cell size threshold was determined from observed diameters of the BioTracker LSFM signal produced by single cells rather than cell clusters. The need for automation of this analysis was intentionally considered when establishing the protocol, so that the binarized cell images could be used to train a deep learning model for faster and more robust 3D segmentation and cell invasion analysis. Due to the volume of LSFM data and computational time required for processing, this makes analyzing 3D cellular invasion from these large image stacks feasible and efficient.

The efficacy of the quantitative analysis of LSFM volumes was demonstrated by detecting the expected significant increases in cell number and invasion depth from day 3 to day 5 within the CRLM biomatrix model. Similarly, capturing the significant reduction in cell number in oxaliplatin-treated samples indicates the ability of LSFM imaging and analysis to detect drug-induced cytotoxic effects (Fig. 7E), which was consistent with the traditional MTS assay (Fig. 3E). These results and their statistical analyses highlight differences in cell invasion patterns across conditions, demonstrating that both temporal progression and oxaliplatin treatment influence cell abundance and invasion within dECM biomatrix samples.

Further, they highlight the value of the presented imaging and analysis pipeline for quantifying metastatic behaviors and treatment responses within dECM models. With our new ability to identify individual cells and accurately quantify the deepest biomatrix invasion, these methods could unlock subtle and nuanced mechanisms of recruitment, migration and drug response.

Mathematical modeling of cellular invasion offers the ability to objectively quantify how deeply and extensively cancer cells metastasize into dECM scaffolds. Fitting cell invasion data to mathematical models such as exponential functions can provide a more accurate and detailed understanding of cancer metastasis, distinguishing between the scale (or amplitude) and rate of invasion. This distinction will be imperative for evaluating cancer cell invasion and distribution within dECM under various experimental conditions, for broader mechanistic discovery. The significant differences in amplitude terms between treated and untreated samples for both single and double exponential fits (Fig. 7) highlight how oxaliplatin limited the extent, but not the rate, of cancer cell invasion.

The integrated whole mount imaging and analysis methods developed in this manuscript hold vast potential for application outside of cancer; in tissue-engineered dECM models used for tissue regeneration, drug delivery, and modeling other disease processes where high-resolution spatially competent cell-matrix phenomena are of interest.

5 Conclusions

In this study, we integrated and optimized advanced sample preparation and optical imaging techniques and invented a custom image analysis protocol to extract precise and quantifiable cellular data from recellularized dECM scaffolds. Application to and analysis of an engineered colorectal cancer liver metastasis model demonstrated its powerful utility for characterizing heterogeneous optically difficult dECM biomaterials. Our methods quantified both biomaterial properties, as well as cell-biomaterial interactions at single-cell resolution. We believe that these image-based analytical methods may increase the adoption and exploration of heterogeneous dECM biomaterials, in cancer discovery and beyond, providing insights into spatially relevant cell-biomaterial interactions.

Author contributions

O. R. B: conceptualization (supporting), data curation (lead), formal analysis (lead), investigation (lead), methodology (lead), software (lead), visualization (lead), writing – original draft (lead), writing – review and editing (lead); S. N. V.: conceptualization (supporting), data curation (lead), formal analysis (lead), investigation (lead), methodology (lead), software (supporting), visualization (lead), writing – original draft (supporting), writing – review and editing (lead); S. R., S. H., B. G., V.



R., J. D., L. L. N.: investigation (supporting); D. L. A.: formal analysis (supporting), methodology (supporting), writing – review and editing (supporting); A. J. W.: conceptualization (lead), formal analysis (supporting), funding acquisition (lead), methodology (lead), project administration (lead), writing – review and editing (supporting); S. A. R.: conceptualization (lead), formal analysis (supporting), funding acquisition (lead), methodology (lead), project administration (lead), writing – review and editing (supporting). O. R. B. and S. N. V. contributed equally to the manuscript by collecting and analyzing data and writing. S. N. V. provided the biological context and generated samples of the established¹ biomatrix model. O. R. B. contributed imaging expertise to optimize imaging parameters and design the image analysis platform. S. A. R. and A. J. W. are shared senior authors.

Conflicts of interest

There are no conflicts to declare.

Data availability

All data (raw imaging data and software codes) used in the manuscript are openly available at github.com/walshlab and the Texas Data Repository with the following <https://doi.org/10.18738/T8/BUCIZS>.

Supplementary information is available including videos for additional visualization as well as data and figures which support the main findings of this study. See DOI: <https://doi.org/10.1039/d5bm00630a>.

Acknowledgements

The authors acknowledge funding by NIH R37CA269224 (SAR, AJW). We thank the Texas A&M University Materials Characterization Core Facility (RRID:SCR_022202) for providing the Thermo Nicolet FTIR spectrometer and the Microscopy and Imaging Center Core Facility (RRID:SCR_022128) for providing the Quanta 600 Field Emission-Scanning Electron Microscope, the Zeiss Z1 Light Sheet Microscope and Imaris image analysis software.

References

- 1 S. N. VandenHeuvel, H. A. Farris, D. A. Noltensmeyer, *et al.*, Decellularized organ biomaterials facilitate quantifiable in vitro 3D cancer metastasis models, *Soft Matter*, 2022, **18**(31), 5791–5806, DOI: [10.1039/D1SM01796A](https://doi.org/10.1039/D1SM01796A).
- 2 D. Bejleri and M. E. Davis, Decellularized Extracellular Matrix Materials for Cardiac Repair and Regeneration, *Adv. Healthcare Mater.*, 2019, **8**(5), e1801217, DOI: [10.1002/adhm.201801217](https://doi.org/10.1002/adhm.201801217).
- 3 H. Amirazad, M. Dadashpour and N. Zarghami, Application of decellularized bone matrix as a bioscaffold in bone tissue engineering, *J. Biol. Eng.*, 2022, **16**(1), 1, DOI: [10.1186/s13036-021-00282-5](https://doi.org/10.1186/s13036-021-00282-5).
- 4 J. Hwang, M. O. Sullivan and K. L. Kiick, Targeted Drug Delivery via the Use of ECM-Mimetic Materials, *Review*, *Front. Bioeng. Biotechnol.*, 2020, **8**, 69, DOI: [10.3389/fbioe.2020.00069](https://doi.org/10.3389/fbioe.2020.00069).
- 5 B. Wang, T. Qinglai, Q. Yang, *et al.*, Functional acellular matrix for tissue repair, *Mater. Today Bio*, 2023, **18**, 100530, DOI: [10.1016/j.mtbiol.2022.100530](https://doi.org/10.1016/j.mtbiol.2022.100530).
- 6 C. Wang, Q. Zhao, X. Zheng, *et al.*, Decellularized brain extracellular matrix slice glioblastoma culture model recapitulates the interaction between cells and the extracellular matrix without a nutrient-oxygen gradient interference, *Acta Biomater.*, 2023, **158**, 132–150, DOI: [10.1016/j.actbio.2022.12.044](https://doi.org/10.1016/j.actbio.2022.12.044).
- 7 E. D'Angelo, D. Natarajan, F. Sensi, *et al.*, Patient-Derived Scaffolds of Colorectal Cancer Metastases as an Organotypic 3D Model of the Liver Metastatic Microenvironment, *Cancers*, 2020, **12**(2), 364, DOI: [10.3390/cancers12020364](https://doi.org/10.3390/cancers12020364).
- 8 E. Oropeza, S. Seker, S. Carrel, *et al.*, Molecular portraits of cell cycle checkpoint kinases in cancer evolution, progression, and treatment responsiveness, *Sci. Adv.*, 2023, **9**(26), eadf2860, DOI: [10.1126/sciadv.adf2860](https://doi.org/10.1126/sciadv.adf2860).
- 9 M. L. Pinto, E. Rios, A. C. Silva, *et al.*, Decellularized human colorectal cancer matrices polarize macrophages towards an anti-inflammatory phenotype promoting cancer cell invasion via CCL18, *Biomaterials*, 2017, **124**, 211–224, DOI: [10.1016/j.biomaterials.2017.02.004](https://doi.org/10.1016/j.biomaterials.2017.02.004).
- 10 D. K. Mishra, M. J. Thrall, B. N. Baird, *et al.*, Human Lung Cancer Cells Grown on Acellular Rat Lung Matrix Create Perfusionable Tumor Nodules, *Ann. Thorac. Surg.*, 2012, **93**(4), 1075–1081, DOI: [10.1016/j.athoracsur.2012.01.011](https://doi.org/10.1016/j.athoracsur.2012.01.011).
- 11 G. Rijal and W. Li, A versatile 3D tissue matrix scaffold system for tumor modeling and drug screening, *Sci. Adv.*, 2017, **3**(9), e1700764, DOI: [10.1126/sciadv.1700764](https://doi.org/10.1126/sciadv.1700764).
- 12 G. Xiong, T. J. Flynn, J. Chen, C. Trinkle and R. Xu, Development of an ex vivo breast cancer lung colonization model utilizing a decellularized lung matrix, *Integr. Biol.*, 2015, **7**(12), 1518–1525, DOI: [10.1039/c5ib00157a](https://doi.org/10.1039/c5ib00157a).
- 13 L. Genovese, L. Zawada, A. Tosoni, *et al.*, Cellular Localization, Invasion, and Turnover Are Differently Influenced by Healthy and Tumor-Derived Extracellular Matrix, *Tissue Eng., Part A*, 2014, **20**(13–14), 2005–2018, DOI: [10.1089/ten.tea.2013.0588](https://doi.org/10.1089/ten.tea.2013.0588).
- 14 Q. L. Loh and C. Choong, Three-dimensional scaffolds for tissue engineering applications: role of porosity and pore size, *Tissue Eng., Part B*, 2013, **19**(6), 485–502, DOI: [10.1089/ten.teb.2012.0437](https://doi.org/10.1089/ten.teb.2012.0437).
- 15 S. Paget, THE DISTRIBUTION OF SECONDARY GROWTHS IN CANCER OF THE BREAST, *Lancet*, 1889, **133**(3421), 571–573, DOI: [10.1016/S0140-6736\(00\)49915-0](https://doi.org/10.1016/S0140-6736(00)49915-0).
- 16 Q. Liu, H. Zhang, X. Jiang, C. Qian, Z. Liu and D. Luo, Factors involved in cancer metastasis: a better understand-



ing to “seed and soil” hypothesis, *Mol. Cancer*, 2017, **16**(1), 176, DOI: [10.1186/s12943-017-0742-4](https://doi.org/10.1186/s12943-017-0742-4).

17 S. Raghavan, P. Mehta, Y. Xie, Y. L. Lei and G. Mehta, Ovarian cancer stem cells and macrophages reciprocally interact through the WNT pathway to promote pro-tumoral and malignant phenotypes in 3D engineered microenvironments, *J. Immunother. Cancer*, 2019, **7**(1), 190, DOI: [10.1186/s40425-019-0666-1](https://doi.org/10.1186/s40425-019-0666-1).

18 S. N. VandenHeuvel, E. Chau, A. Mohapatra, *et al.*, Macrophage Checkpoint Nanoimmunotherapy Has the Potential to Reduce Malignant Progression in Bioengineered In Vitro Models of Ovarian Cancer, *ACS Appl. Bio Mater.*, 2024, **7**(12), 7871–7882, DOI: [10.1021/acsabm.4c00076](https://doi.org/10.1021/acsabm.4c00076).

19 N. Renier, Z. Wu, D. J. Simon, J. Yang, P. Ariel and M. Tessier-Lavigne, iDISCO: A Simple, Rapid Method to Immunolabel Large Tissue Samples for Volume Imaging, *Cell*, 2014, **159**(4), 896–910, DOI: [10.1016/j.cell.2014.10.010](https://doi.org/10.1016/j.cell.2014.10.010).

20 M. Habart, G. Lio, A. Soumier, C. Demilly and A. Sirigu, An optimized iDISCO+ protocol for tissue clearing and 3D analysis of oxytocin and vasopressin cell network in the developing mouse brain, *STAR Protoc.*, 2023, **4**(1), 101968, DOI: [10.1016/j.xpro.2022.101968](https://doi.org/10.1016/j.xpro.2022.101968).

21 F. L. Jalufka, S. W. Min, M. E. Platt, *et al.*, Hydrophobic and Hydrogel-Based Methods for Passive Tissue Clearing, *Methods Mol. Biol.*, 2022, **2440**, 197–209, DOI: [10.1007/978-1-0716-2051-9_12](https://doi.org/10.1007/978-1-0716-2051-9_12).

22 D. A. McCready, F. L. Jalufka, M. E. Platt, *et al.*, Passive Clearing and 3D Lightsheet Imaging of the Intact and Injured Spinal Cord in Mice. Methods, *Front. Cell. Neurosci.*, 2021, **15**, 684792, DOI: [10.3389/fncel.2021.684792](https://doi.org/10.3389/fncel.2021.684792).

23 T. W. Ridler and S. Calvard, Picture Thresholding Using an Iterative Selection Method, *IEEE Trans. Syst., Man, Cybernetics*, 1978, **8**(8), 630–632, DOI: [10.1109/TSMC.1978.4310039](https://doi.org/10.1109/TSMC.1978.4310039).

24 M. H. Santos, R. M. Silva, V. C. Dumont, J. S. Neves, H. S. Mansur and L. G. Heneine, Extraction and characterization of highly purified collagen from bovine pericardium for potential bioengineering applications, *Mater. Sci. Eng., C*, 2013, **33**(2), 790–800, DOI: [10.1016/j.msec.2012.11.003](https://doi.org/10.1016/j.msec.2012.11.003).

25 T. Riaz, R. Zeeshan, F. Zarif, *et al.*, FTIR analysis of natural and synthetic collagen, *Appl. Spectrosc. Rev.*, 2018, **53**(9), 703–746, DOI: [10.1080/05704928.2018.1426595](https://doi.org/10.1080/05704928.2018.1426595).

26 B. de Campos Vidal and M. L. S. Mello, Collagen type I amide I band infrared spectroscopy, *Micron*, 2011, **42**(3), 283–289, DOI: [10.1016/j.micron.2010.09.010](https://doi.org/10.1016/j.micron.2010.09.010).

27 M. L. D. P. Audelo, K. K. G. Lizárraga, D. Mauricio, *et al.*, Development of collagen-EDC scaffolds for skin tissue engineering: physicochemical and biological characterization, *Int. J. Eng. Res. Sci.*, 2016, **2**(4), 73–83.

28 Y. Zhou, C. Chen, Z. Guo, S. Xie, J. Hu and H. Lu, SR-FTIR, as a tool for quantitative mapping of the content and distribution of extracellular matrix in decellularized book-shape bioscaffolds, *BMC Musculoskeletal Dis.*, 2018, **19**(1), 220, DOI: [10.1186/s12891-018-2149-9](https://doi.org/10.1186/s12891-018-2149-9).

29 K. J. Zuiderveld, *Contrast Limited Adaptive Histogram Equalization*, 1994.

30 A. F. Frangi, W. J. Niessen, K. L. Vincken and M. A. Viergever, *Multiscale vessel enhancement filtering*, Springer, Berlin Heidelberg, 1998, pp. 130–137.

31 T. Yu, J. Zhu, D. Li and D. Zhu, Physical and chemical mechanisms of tissue optical clearing, *iScience*, 2021, **24**(3), 102178, DOI: [10.1016/j.isci.2021.102178](https://doi.org/10.1016/j.isci.2021.102178).

32 J. G. Scott, P. Gerlee, D. Basanta, A. G. Fletcher, P. K. Maini and A. R. A. Anderson, Mathematical Modeling of the Metastatic Process, in *Experimental Metastasis: Modeling and Analysis*, ed. A. Malek, Springer, Netherlands, 2013, pp. 189–208.

33 A. E. Mayorca-Guiliani, O. Willacy, C. D. Madsen, *et al.*, Decellularization and antibody staining of mouse tissues to map native extracellular matrix structures in 3D, *Nat. Protoc.*, 2019, **14**(12), 3395–3425, DOI: [10.1038/s41596-019-0225-8](https://doi.org/10.1038/s41596-019-0225-8).

34 S. Batasheva, K. Svetlana, F. Anastasia and R. Fakhrullin, Atomic force microscopy for characterization of decellularized extracellular matrix (dECM) based materials, *Sci. Technol. Adv. Mater.*, 2024, **25**(1), 2421739, DOI: [10.1080/14686996.2024.2421739](https://doi.org/10.1080/14686996.2024.2421739).

35 J. Liao, B. Xu, R. Zhang, Y. Fan, H. Xie and X. Li, Applications of decellularized materials in tissue engineering: advantages, drawbacks and current improvements, and future perspectives, *J. Mater. Chem. B*, 2020, **8**(44), 10023–10049, DOI: [10.1039/D0TB01534B](https://doi.org/10.1039/D0TB01534B).

36 A. E. Mayorca-Guiliani, C. D. Madsen, T. R. Cox, E. R. Horton, F. A. Venning and J. T. Erler, ISDoT: in situ decellularization of tissues for high-resolution imaging and proteomic analysis of native extracellular matrix, *Nat. Med.*, 2017, **23**(7), 890–898, DOI: [10.1038/nm.4352](https://doi.org/10.1038/nm.4352).

37 B. Oberwallner, A. Brodarac, Y.-H. Choi, *et al.*, Preparation of cardiac extracellular matrix scaffolds by decellularization of human myocardium, *J. Biomed. Mater. Res., Part A*, 2014, **102**(9), 3263–3272, DOI: [10.1002/jbm.a.35000](https://doi.org/10.1002/jbm.a.35000).

38 D. H. Ramos-Rodriguez, S. W. Fok, C. J. Dorais, A. C. Filler, M. Caserta and J. K. Leach, Decellularized Extracellular Matrix Improves Mesenchymal Stromal Cell Spheroid Response to Chondrogenic Stimuli, *Tissue Eng., Part A*, 2024, **31**(3–4), 139–151, DOI: [10.1089/ten.tea.2024.0267](https://doi.org/10.1089/ten.tea.2024.0267).

39 C.-M. Hsieh, W. Wang, Y.-H. Chen, *et al.*, A Novel Composite Hydrogel Composed of Formic Acid-Decellularized Pepsin-Soluble Extracellular Matrix Hydrogel and Sacchachitin Hydrogel as Wound Dressing to Synergistically Accelerate Diabetic Wound Healing, *Pharmaceutics*, 2020, **12**(6), 538.

40 R. D. Ventura, A. R. Padalhin, C. M. Park and B. T. Lee, Enhanced decellularization technique of porcine dermal ECM for tissue engineering applications, *Mater. Sci. Eng., C*, 2019, **104**, 109841, DOI: [10.1016/j.msec.2019.109841](https://doi.org/10.1016/j.msec.2019.109841).

41 T. Mimler, C. Nebert, E. Eichmair, *et al.*, Extracellular matrix in ascending aortic aneurysms and dissections – What we learn from decellularization and scanning elec-



tron microscopy, *PLoS One*, 2019, **14**(3), e0213794, DOI: [10.1371/journal.pone.0213794](https://doi.org/10.1371/journal.pone.0213794).

42 R. A. Behmer Hansen, X. Wang, G. Kaw, V. Pierre and S. E. Senyo, Accounting for Material Changes in Decellularized Tissue with Underutilized Methodologies, *BioMed Res. Int.*, 2021, **2021**(1), 6696295, DOI: [10.1155/2021/6696295](https://doi.org/10.1155/2021/6696295).

43 M. Brown, J. Li, C. Moraes, M. Tabrizian and N. Y. K. Li-Jessen, Decellularized extracellular matrix: New promising and challenging biomaterials for regenerative medicine, *Biomaterials*, 2022, **289**, 121786, DOI: [10.1016/j.biomaterials.2022.121786](https://doi.org/10.1016/j.biomaterials.2022.121786).

44 P. Maghsoudlou, F. Georgiades, A. Tyraskis, *et al.*, Preservation of micro-architecture and angiogenic potential in a pulmonary acellular matrix obtained using intermittent intra-tracheal flow of detergent enzymatic treatment, *Biomaterials*, 2013, **34**(28), 6638–6648, DOI: [10.1016/j.biomaterials.2013.05.015](https://doi.org/10.1016/j.biomaterials.2013.05.015).

45 M. Stefaniuk, E. J. Gualda, M. Pawlowska, *et al.*, Light-sheet microscopy imaging of a whole cleared rat brain with Thy1-GFP transgene, *Sci. Rep.*, 2016, **6**, 28209, DOI: [10.1038/srep28209](https://doi.org/10.1038/srep28209).

46 R. Cai, C. Pan, A. Ghasemigharagoz, *et al.*, Panoptic imaging of transparent mice reveals whole-body neuronal projections and skull-meninges connections, *Nat. Neurosci.*, 2019, **22**(2), 317–327, DOI: [10.1038/s41593-018-0301-3](https://doi.org/10.1038/s41593-018-0301-3).

47 C. Brenna, C. Simioni, G. Varano, *et al.*, Optical tissue clearing associated with 3D imaging: application in pre-clinical and clinical studies, *Histochem. Cell Biol.*, 2022, **157**(5), 497–511, DOI: [10.1007/s00418-022-02081-5](https://doi.org/10.1007/s00418-022-02081-5).

48 J. P. Ritz, A. Roggan, C. Isbert, G. Muller, H. J. Buhr and C. T. Germer, Optical properties of native and coagulated porcine liver tissue between 400 and 2400 nm, *Lasers Surg. Med.*, 2001, **29**(3), 205–212, DOI: [10.1002/lsm.1134](https://doi.org/10.1002/lsm.1134).

49 K. O. Oyebode and J. R. Tapamo, Automatic Segmentation of Cell Images by Improved Graph Cut-Based Approach, *J. Biomimetics, Biomater. Biomed. Eng.*, 2016, **29**, 74–80, DOI: [10.4028/www.scientific.net/JBBBE.29.74](https://doi.org/10.4028/www.scientific.net/JBBBE.29.74).

50 L. Zhang, H. Kong, C. T. Chin, T. Wang and S. Chen, Cytoplasm segmentation on cervical cell images using graph cut-based approach, *Bio-Med. Mater. Eng.*, 2014, **24**, 1125–1131, DOI: [10.3233/BME-130912](https://doi.org/10.3233/BME-130912).

51 N. O. Loewke, S. Pai, C. Cordeiro, *et al.*, Automated Cell Segmentation for Quantitative Phase Microscopy, *IEEE Trans. Med. Imaging*, 2018, **37**(4), 929–940, DOI: [10.1109/TMI.2017.2775604](https://doi.org/10.1109/TMI.2017.2775604).

52 E. Decencière, E. Tancrède-Bohin, P. Dokládal, S. Koudoro, A.-M. Pena and T. Baldeweck, Automatic 3D segmentation of multiphoton images: a key step for the quantification of human skin, *Skin Res. Technol.*, 2013, **19**(2), 115–124, DOI: [10.1111/srt.12019](https://doi.org/10.1111/srt.12019).

53 N. Renier, E. L. Adams, C. Kirst, *et al.*, Mapping of Brain Activity by Automated Volume Analysis of Immediate Early Genes, *Cell*, 2016, **165**(7), 1789–1802, DOI: [10.1016/j.cell.2016.05.007](https://doi.org/10.1016/j.cell.2016.05.007).

54 K. Hajdowska, S. Student and D. Borys, Graph based method for cell segmentation and detection in live-cell fluorescence microscope imaging, *Biomed. Signal Process. Control*, 2022, **71**, 103071, DOI: [10.1016/j.bspc.2021.103071](https://doi.org/10.1016/j.bspc.2021.103071).

55 H. Chen and R. F. Murphy, Evaluation of cell segmentation methods without reference segmentations, *Mol. Biol. Cell*, 2023, **34**(6), ar50, DOI: [10.1091/mbc.E22-08-0364](https://doi.org/10.1091/mbc.E22-08-0364).

56 S. Berg, D. Kutra, T. Kroeger, *et al.*, ilastik: interactive machine learning for (bio)image analysis, *Nat. Methods*, 2019, **16**(12), 1226–1232, DOI: [10.1038/s41592-019-0582-9](https://doi.org/10.1038/s41592-019-0582-9).

57 U. Schmidt, M. Weigert, C. Broaddus and G. Myers, *Cell Detection with Star-Convex Polygons*, Springer International Publishing, 2018, pp. 265–273.

58 M. Weigert, U. Schmidt, R. Haase, K. Sugawara and G. Myers, Star-convex Polyhedra for 3D Object Detection and Segmentation in Microscopy, 2020, pp. 3655–3662.

59 M. Weigert and U. Schmidt, Nuclei Instance Segmentation and Classification in Histopathology Images with Stardist, 2022, pp. 1–4.

60 K. N. Lama, B. M. Moustapha and T. Ali, White Blood Cells Detection Using Spectral Tresholding, *J. Signal Inf. Process.*, 2023, **14**(1), 1–8.

61 H. S. Wu, J. Barba and J. Gil, An iterative algorithm for cell segmentation using short-time Fourier transform, *J. Microsc.*, 1996, **184**(Pt 2), 127–132, DOI: [10.1111/j.1365-2818.1996.tb00007.x](https://doi.org/10.1111/j.1365-2818.1996.tb00007.x).

